Computer Methods in Applied Mechanics and Engineering 446 (2025) 118275

Contents lists available at ScienceDirect

Comput. Methods Appl. Mech. Engrg.

journal homepage: www.elsevier.com/locate/cma

Assessment of isotropic large-deformation elastoplasticity models with Lode angle dependence

Andrea Panteghini [a,*], M. B. Rubin [b], Lorenzo Bardella [a]

[a] Department of Civil, Environmental, Architectural Engineering and Mathematics, University of Brescia, Italy
[b] Faculty of Mechanical Engineering, Technion-Israel Institute of Technology, Haifa, 32000, Israel

ARTICLE INFO

Keywords:
Lode angle
Large deformations
Eulerian constitutive equations
Isotropic elastoplasticity
Finite element method

ABSTRACT

This study aims at assessing formulations of large-deformation elastoplasticity dependent on the Lode angle. The focus is both on the accuracy of the predictions and on the computational efficiency. Although the analysis is limited to isotropic response and isochoric plastic deformation, the proposed assessment has required the extension of an Eulerian model relying on the left Cauchy-Green elastic strain, to include the influence of the Lode angle in the plastic rate tensor. Also, the computational algorithm for more commonly implemented models, derived by assuming the Bilby-Kröner-Lee multiplicative form of the deformation gradient and adopting the logarithmic strain measure, has been significantly improved by using a relatively accurate approximate derivative of the logarithmic strain. While the models implemented in this study assume hyperelasto-plastic behavior, the assessment also includes the hypoelasto-plastic model available in the commercial finite element code Abaqus. For all the specified constitutive equations, some numerical algorithms for small-deformation elastoplasticity can be used for finite deformations. Conclusions are drawn on the basis of some analysis and three benchmark problems, i.e. plane-strain cyclic shearing of a square block, necking of a circular cylindrical bar, and drawing of a bar with a rectangular cross-section. All these problems consider both von Mises plasticity and Tresca plasticity, the latter leading to significant differences among the models in terms of the Lode angle, mostly under plane-strain conditions. The main result is that the considered models overall provide similar engineering responses, but the numerical efficiency of the Eulerian model relying on the left Cauchy-Green elastic strain and the ease of its implementation have advantages over the other models.

1. Introduction

This study focuses on the comparison of different formulations of large-deformation elastoplasticity dependent on the Lode angle. The assessment concerns both the results and the numerical performance. To this end, the analysis is limited to isotropic response.

1.1. Brief overview on yield surfaces dependent on the Lode angle

Since the pioneering contributions of Coulomb [9] and Tresca [77], isotropic failure surfaces dependent on von Mises stress, pressure, and Lode angle have been developed by several investigators. Specifically, in soil mechanics, the dependence on the third

* Corresponding author.
E-mail addresses: andrea.panteghini@unibs.it (A. Panteghini), mbrubin@tx.technion.ac.il (M. B. Rubin), lorenzo.bardella@ing.unibs.it (L. Bardella).

https://doi.org/10.1016/j.cma.2025.118275
Received 1 April 2025; Received in revised form 2 July 2025; Accepted 27 July 2025
Available online 6 August 2025

invariant goes back to the Mohr-Coulomb criterion [9,44], in which the yield surface depends exclusively on the maximum and minimum principal stresses. The influence of the intermediate principal stress (and then, of the Lode angle) has been experimentally investigated by Lade and Duncan [33], leading to the development of further criteria, such as those of Lade and Duncan [34] and of Matsuoka and Nakai [42], or the extension of the latter to cohesive soil proposed by Houlsby [22]. Moreover, for general quasi-brittle materials the need to include the influence of the Lode angle in addition to accounting for the stress triaxiality is well established since the Seventies (e.g. van Eekelen [13], Jaeger and Cook [24], Lade [31,32], Ottosen [48], Panteghini and Lagioia [51], William and Warnke [79]). More recent studies have shown that the same need holds for metals, mostly because of the crucial role of voids' growth and coalescence in the initiation of macroscopic fracture.

Specifically, Nahshon and Hutchinson [46] discuss the limitations of using stress triaxiality alone to characterize ductile fracture, highlighting the need to account for the Lode angle and proposing an extension of the Gurson criterion [17] to model shear-dominated damage growth. Experiments on circumferentially notched tubes constituted by either mid-strength or high-strength Weldox steel under combined tension and torsion [4] have contributed to clarify the roles of stress triaxiality and Lode angle, the latter being e.g. important to distinguish between plane-strain and axisymmetric stress states; Barsoum and Faleskog [4] have also observed increased susceptibility to fracture under low-triaxiality shearing conditions. FE computations on representative material elements including initially spherical voids and subjected to various stress states [5,14] have also demonstrated that stress triaxiality alone is insufficient to fully characterize void growth rates and other key aspects of void behavior related to material softening and localization, emphasizing the critical role played by the Lode angle. In order to fit the results of mechanical tests in the plastic regime on certain metals such as aluminum 2024-T351 and A710 steel, Bai and Wierzbicki [2] have proposed a yield surface (later modified by Vershinin [78]) dependent on von Mises stress, pressure, and Lode angle.

Among others, Kroon and Faleskog [29] have developed a yield function dependent on von Mises stress and Lode angle with the purpose of continuously parametrizing, through a material constant, yield surfaces within those of von Mises and Tresca; however, the adopted technique uses a power-law that may lead to numerical issues [11,29]. The theoretical studies in Bardet [3], Bigoni and Piccolroaz [7], Lagioia and Panteghini [36], Panteghini and Lagioia [52], Piccolroaz and Bigoni [55], Podgórski [56], Rubin [58,62], among others, have shown how to conveniently represent yield surfaces dependent on von Mises stress, pressure, and Lode angle. Specifically, the yield surface in [52] is *fully convex*, meaning that convexity is retained when the surface expands to pass through stress points outside the current elastic domain, which is beneficial in predictor-corrector numerical schemes.

In this investigation, where the focus is on an initial basic assessment of models for finite-deformation elastoplasticity, attention is limited to pressure-independent yield functions, specifically ignoring dilatational plasticity. Nevertheless, this work adopts a yield function that can be specialized to several classical criteria, including von Mises, Galileo, and smooth approximations of Tresca and Mohr-Coulomb, as proposed in [52].

1.2. Short summary of the literature on formulations for isotropic finite-deformation elastoplasticity

In the absence of inelasticity, the formulation of large-deformation elasticity and solutions of a number of fundamental problems can be found in the collected works of Rivlin and Barenblatt [57]. In the literature, elastically isotropic response can be described as either hypoelastic or hyperelastic. In the case of hypoelasticy, the stress is determined by an evolution equation which proposes that an objective rate of stress ([54], and references therein) depends linearly on the total rate of deformation tensor $\mathbf{D}$, with elastic moduli that may depend on stress. In contrast, for hyperelastic response, the stress is determined by the derivative of a strain energy function, such that the work done between any two total strain states is path-independent. For hypoelastic response to be path-independent it is necessary that the constitutive equation satisfies integrability conditions [6].

One of the very first contributions to modelling finite-deformation elastoplasticity is due to Hill [21]. Hypoelastic constitutive equations have been generalized for hypoelasto-plastic response by substituting $\mathbf{D}$ with an elastic rate $\mathbf{D}_e = \mathbf{D} - \mathbf{D}_p$, where $\mathbf{D}_p$ is a plastic rate. The hypoelastic case needs to be discussed not only for historical reasons, as it has been the first approach systematically investigated (see, e.g., Argyris and Kleiber [1], Hibbitt et al. [20], McMeeking and Rice [43], Nagtegaal and De Jong [45]), but also because several commercial finite element (FE) codes for isotropic large-deformation elastoplastic response still adopt it. Yet, these models are employed in recent applicative investigations, encompassing geotechnique [67], metal failure under multiaxial repeated loadings [81], and dislocation density-based crystal plasticity [80]. However, *additive hypoelasto-plasticity models may be affected by path-dependent predictions* in the absence of inelasticity [75].

Hyperelastic models for elastoplastic response typically propose a Lagrangian constitutive equation for the stress. This formulation may rely either on a plastic deformation tensor $\mathbf{C}_p$ (see Green and Naghdi [16], for more details), or on the mulitiplicative form $\mathbf{F} = \mathbf{F}_e\mathbf{F}_p$ [8,28,38] which defines the elastic deformation gradient as

$$\mathbf{F}_e \equiv \mathbf{F}\mathbf{F}_p^{-1}, \tag{1}$$

where $\mathbf{F}$ it the total deformation gradient from a reference configuration to the current configuration, while $\mathbf{F}_p$ is the plastic deformation tensor from the reference configuration to an intermediate configuration, such that $\mathbf{F}_e$ maps the intermediate configuration into the current configuration. This formulation is the most widely adopted in the literature and it has become popular since the mid Eighties, with works, such as Simo and Ortiz [74], aiming at proposing *multiplicative hyperelasto-plasticity models* to address issues raised about hypoelasto-plasticity. The book chapter [71] and the book [11] provide excellent overviews of this formulation, also with reference to its FE implementation. Constitutive models of this type are *usually* denoted as Lagrangian because they depend on $\mathbf{F}$, and an evolution equation on either the plastic right Cauchy-Green tensor $\mathbf{C}_p$ or the plastic deformation $\mathbf{F}_p$, as well a definition of $\mathbf{F}_e$.

For a more recent and detailed comparative review of additive hypoelasto-plasticity and multiplicative hyperelasto-plasticity models, the reader is referred to the contributions of Jiao and Fish [25,26]. Additionally, Jiao and Fish [26] have demonstrated that, for isotropic materials, the additive hypoelasto-plasticity model based on the modified kinetic logarithmic stress rate proposed in [25] coincides with a multiplicative hyperelasto-plasticity model adopting the logarithmic strain [19]. The logarithmic strain measure is widely used in this framework for the reasons explained in de Souza Neto et al. [11].

This investigation also considers the Eulerian formulation discussed in Rubin [61], which relies on the work in Eckart [12], Leonov [39] and follows Onat [47]. Its crucial feature is that it assumes that the constitutive equations may depend exclusively on state variables that are measurable in the current state, which is not the case for $\mathbf{F}_e$ and $\mathbf{F}_p$. Consequently, this formulation is insensitive to the arbitrariness inherent in most Lagrangian formulations relying on Eq. (1), such as the definition of an intermediate configuration [60].

Eulerian formulations for elastically isotropic response have been proposed both for conventional plasticity [63,65] and, more recently, for size-dependent plasticity [64]. In some cases, these models have been obtained by specializing more general elastically anisotropic constitutive equations developed since the proposal in Rubin [59].

Additionally, within this Eulerian framework, the strongly objective nature of numerical algorithms employed to solve the evolution equations for elastic deformations has been discussed in Jabareen [23], Rubin and Papes [66], where use is made of the relative deformation gradient for numerical integration of the elastic trial value of elastic deformation [69]. Following Rubin and Attia [63], evolution equations are proposed for the elastic dilatation J_e and a symmetric unimodular elastic distortional deformation tensor $\bar{\mathbf{B}}_e$, with the distortional plastic rate being proportional to a symmetric second-order tensor $\mathbf{A}_p$. This formulation conveniently adopts the left Cauchy-Green strain measure based on $\bar{\mathbf{B}}_e$.

In contrast to the case of general anisotropic response, it has been shown that for isotropic response it is possible to develop Eulerian formulations of evolution equations which remove the arbitrariness in the general equations of the multiplicative formulation (e.g. de Souza Neto et al. [11], Simo [68], Simo and Miehe [73]). This is detailed in Section 3.1, which also reviews different Eulerian formulations. Included are the formulations in Eckart [12], Leonov [39], Simo [68], Simo and Miehe [73], the formulation in Rubin and Attia [63], here denoted as the B_e model, as well as the formulation summarized in Boxes 14.3 and 14.4 in de Souza Neto et al. [11], ensuing from the multiplicative form (1) and using the logarithmic strain, that is the basis for the models here denoted as LN and LN-MD. Note that, at the time of the developments in Simo [68], Simo and Miehe [73], the physical importance of Eulerian formulations [61] was not fully recognized.

Recently, Kumar and Patel [30] have combined the Eulerian formulation of Simo and Miehe [73] with the yield surfaces proposed in Kroon and Faleskog [29] and Vershinin [78], in order to establish the computational performance of the time-integration schemes developed by Simo [70] and Geers [15]. Results have been discussed on the basis of applications to the modeling of grooved plates constituted by isotropic metal.

1.3. Contributions of this investigation

Achieving the goal of this investigation has led to new developments. One of them is deriving the form of the tensor $\mathbf{A}_p$ to include the influence of the Lode angle on the direction of the rate of plasticity in the adopted Eulerian formulation, consistently with the selected yield function [52]. The small-deformation limit of the proposed Eulerian formulation reduces to an associated flow rule.

Notably, the dependence of the direction of the rate of plasticity on the Lode angle adds complexity in the integration of elasto-plastic models, because the derivative of the Lode angle with respect to the stress tensor is undefined when two principal stress components coincide. To address this issue, the return mapping algorithm should not be formulated in terms of the elastic tensor/stress components, as is commonly accomplished, but rather in terms of stress invariants, leveraging isotropy. Accordingly, this work employs a return mapping algorithm originally proposed by Panteghini and Lagioia [51] and later extended in [52] to arbitrary isotropic yield functions, and in [53] to a Cosserat medium.

Another objective of this study is to show that some numerical algorithms developed for small-deformation elastoplasticity can be employed to model large-deformation elastoplasticity not only in the specific hyperelasto-plasticity model based on logarithmic strain adopted here (see de Souza Neto et al. [11], Simo [71], and references therein), but also in the Eulerian framework of [63], based on the left Cauchy-Green elastic strain $\boldsymbol{\varepsilon}_e$. Specifically, by assuming a special form of a strain-energy function for compressible Neo-Hookean response that is valid for large deformations, it is shown that for the Eulerian formulation based on $\bar{\mathbf{B}}_e$ (denoted as the B_e model), the Kirchhoff stress $\boldsymbol{\tau}$ is given by[1]

$$\boldsymbol{\tau} = K\,\mathrm{tr}(\boldsymbol{\varepsilon}_e)\mathbf{I} + 2\mu\boldsymbol{\varepsilon}'_e, \tag{2}$$

where K and μ are the zero-stress bulk and shear moduli, respectively, and the elastic strain $\boldsymbol{\varepsilon}_e$ is defined by

$$\boldsymbol{\varepsilon}_e = \frac{J_e - 1}{3}\mathbf{I} + \boldsymbol{\varepsilon}'_e, \quad \boldsymbol{\varepsilon}'_e = \frac{1}{2}\bar{\mathbf{B}}'_e, \tag{3}$$

where $\boldsymbol{\alpha}'$ denotes the deviatoric part of a general second-order tensor $\boldsymbol{\alpha}$, such that

$$\boldsymbol{\varepsilon}'_e = \boldsymbol{\varepsilon}_e - \frac{1}{3}\mathrm{tr}(\boldsymbol{\varepsilon}_e)\mathbf{I}\,. \tag{4}$$

[1] Here and henceforth, $\mathrm{tr}(\mathbf{A}) = \mathbf{A}\cdot\mathbf{I}$, where $\mathbf{I}$ denotes the second-order identity tensor and $\mathbf{A}\cdot\mathbf{B} = \mathrm{tr}(\mathbf{A}\mathbf{B}^T)$ is the inner product of two second-order tensors $\mathbf{A}, \mathbf{B}$. Also, $|\mathbf{C}| = \sqrt{\mathbf{C}\cdot\mathbf{C}}$ and $\bar{\mathbf{C}} \equiv \det(\mathbf{C})^{-1/3}\mathbf{C}$ are, respectively, the magnitude and the unimodular part of the tensor $\mathbf{C}$.

It is emphasized that the constitutive equation for $\boldsymbol{\tau}$ in (2) is valid for large deformations. This notwithstanding, its linear structure allows for the use of some small-deformation routines even in the finite-deformation framework. Also, it is mentioned that $\mathrm{tr}(\boldsymbol{\varepsilon}_e)$ is a pure measure of elastic dilatation and $\boldsymbol{\varepsilon}'_e$ is a pure measure of elastic distortional deformation.

This work uses the commercial FE code Abaqus [10], whose built-in hypoelastic formulation is here denoted as the HYPO model. The hyperelasto-plastic model based on the multiplicative form in Eq. (1) and Hencky's strain [11] is denoted as the LN model, and its 2D implementation uses the coding in de Souza Neto et al. [11]. The hyperelasto-plastic models discussed in this paper are elastically isotropic with the strain energy function being an isotropic function of elastic deformation and they are plastically isotropic with the direction of the rate of plasticity also being an isotropic function of elastic deformation. Both the HYPO and the LN models adopt constitutive equations requiring the computation of the logarithm of a symmetric positive-definite second-order tensor to determine the strain. Specifically, the HYPO model in Abaqus computes the logarithm of the increment of the left stretch tensor, while the LN model computes Hencky's logarithmic elastic strain. de Souza Neto et al. [11] explain the reason for using Hencky's elastic strain in the LN model. Specifically, equations (14.77) and (14.80) in [11] show that for general elastic strains the numerical integration of the evolution equation for $\mathbf{F}_p$ requires an exponential map as well as the polar decomposition of $\mathbf{F}_e$. However, the complications of the exponential map are eliminated by limiting attention to logarithmic elastic strains (see equation (14.89) in de Souza Neto et al. [11]). As already mentioned, Section 3.1 shows that this also leads to an Eulerian formulation of the constitutive equations for elastic deformation and stress.

Implementations of the LN model usually employ a spectral representation that is markedly sensitive to numerical errors, especially for the derivative of the logarithm when two eigenvalues are equal or nearly equal. To address this issue, this investigation develops a significantly improved computational algorithm, which holds for 3D simulations, by combining exact values of projection operators with exact values of rates of the eigenvalues obtained by an approximate derivative of the logarithmic strain. This modified model is denoted as the LN-MD model. This work shows that the LN-MD model is more efficient than the LN model.

In this investigation the LN, LN-MD, and B_e models are implemented in user element (`uel`) subroutines for Abaqus, thus employing exactly the same FE formulation for all of them. Instead, the HYPO model uses the corresponding finite elements available in the Abaqus library, and a user material (`umat`) subroutine is implemented for the case of Tresca plasticity.

The differences between the Neo-Hookean response, here concerned with the B_e model, and the predictions of the Hencky response, here concerned with the LN and LN-MD models, will be preliminarily analyzed by focusing on the large-deformation elastic response to simple shear. Then, benchmark problems of plane-strain cyclic shearing of a square block, necking of a circular cylindrical bar, and drawing of a bar with a rectangular cross-section are used to assess the models considered, in terms of efficiency and accuracy. Differences in the predictions are significant for elastic response with large elastic strains, but are relative small for elastoplastic response with small elastic strains. The B_e model, although being hyperelasto-plastic, is not based on logarithmic strain, so it is simpler to implement than the other models considered, while retaining accuracy and being computationally efficient.

An outline of the paper is as follows. After introducing in Section 2 some basic equations of isochoric plasticity and elastically isotropic response, including the yield function that depends on the Lode angle, Section 3 summarizes the basic equations that differ between the B_e model and the LN, LN-MD models, with focus on elastic deformation measures. The B_e model is presented in more detail since this model is less known and since the direction of the rate of plasticity is being modified to include Lode angle dependence. In this regard, Section 4 develops the modified direction of plastic rate and the hardening for the B_e model, including the proof of non-negative dissipation rate. Section 5 presents a time-integration algorithm of the constitutive equations that holds for all the finite-deformation models considered in this work. Section 6 summarizes the FE formulation including the computation of residuals and the equations for the consistent tangent matrix. Section 7 compares the efficiency and accuracy of the four models considered, by discussing the results obtained for the benchmark problems. Section 8 presents the concluding remarks.

2. Some basic equations with focus on isochoric plastic deformation and elastically isotropic response

2.1. Kinematics

The velocity $\mathbf{v}$ of the material point located at $\mathbf{x}$ in the current configuration is given by

$$\mathbf{v} = \dot{\mathbf{x}}, \tag{5}$$

where $\dot{(\,)}$ denotes material time differentiation. Also, the velocity gradient $\mathbf{L}$ and the rate of deformation $\mathbf{D}$ are defined by

$$\mathbf{L} = \partial \mathbf{v}/\partial \mathbf{x}, \quad \mathbf{D} = \frac{1}{2}(\mathbf{L} + \mathbf{L}^T). \tag{6}$$

2.2. Elastic dilatation

In the absence of dilatational plasticity, the elastic dilatation J_e satisfies the evolution equation

$$\frac{\dot{J}_e}{J_e} = \mathrm{tr}(\mathbf{D}). \tag{7}$$

Using the conservation of the mass, the elastic dilatation J_e can be expressed in terms of the current mass density ρ and the zero-stress mass density ρ_z, such that

$$J_e = \frac{\rho_z}{\rho}. \tag{8}$$

Table 1
Material parameters for $G(\theta)$ in Eq. (15) to reproduce the yield criteria adopted in this work [36].

Criterion	b	c	a
von Mises	0	0	1
Compression cut-off	1	2	1
Tension cut-off (Rankine)	1	0	2
(outer) rounded Tresca	0.9999	1	$\left\{\sin\left[(\pi+\arccos b)/3\right]\right\}^{-1} \approx 1.15158$

2.3. The Cauchy stress and an effective elastic distortional strain

It is convenient to use the relation between the Cauchy stress $\mathbf{T}$ and the Kirchhoff stress $\boldsymbol{\tau}$ (e.g. de Souza Neto et al. [11]),

$$\boldsymbol{\tau} = J_e \mathbf{T}, \tag{9}$$

to write the deviatoric parts of the Cauchy and Kirchhoff stresses in the forms

$$\mathbf{T}' = 2J_e^{-1}\mu\boldsymbol{\mathcal{E}}'_e, \quad \boldsymbol{\tau}' = 2\mu\boldsymbol{\mathcal{E}}'_e, \tag{10}$$

where $\boldsymbol{\mathcal{E}}'_e$ is a deviatoric elastic strain, which is equal to $\boldsymbol{\epsilon}'_e$ in Eq. (3) for the B_e model or to $\mathbf{E}'_e$ for the LN and LN-MD models, $\mathbf{E}'_e$ being defined later in Section 3.3.

Moreover, it follows that the equivalent von Mises stress σ_e is given by

$$\sigma_e = \sqrt{3/2}|\mathbf{T}'| = 3J_e^{-1}\mu\varepsilon_{eq}, \tag{11}$$

where

$$\varepsilon_{eq} = \sqrt{2/3}|\boldsymbol{\mathcal{E}}'_e| \tag{12}$$

is the equivalent elastic distortional strain associated with Kirchhoff deviatoric stress $\boldsymbol{\tau}'$.

2.4. Lode angle

Since the deviatoric part of the Cauchy stress tensor is proportional to $\boldsymbol{\mathcal{E}}'_e$, the standard definition of the Lode angle based on the deviatoric stress [40] can be expressed either as a function of $\boldsymbol{\tau}'$ or as a function of $\boldsymbol{\mathcal{E}}'_e$,

$$\sin(3\theta) = -\frac{3\sqrt{6}\det(\boldsymbol{\tau}')}{|\boldsymbol{\tau}'|^3} = -\frac{27\det(\boldsymbol{\mathcal{E}}'_e)}{2\gamma_e^3}, \quad -\frac{\pi}{6} \le \theta \le \frac{\pi}{6}, \quad \text{with} \quad \gamma_e = \frac{3}{2}\varepsilon_{eq}, \tag{13}$$

where use has been made of Eqs. (10) and (12).

2.5. Yield function

Panteghini and Lagioia [52] developed a yield function dependent on the Lode angle θ that provides a smooth approximation of the original Tresca and Mohr–Coulomb criteria, among other classical criteria. A special case of this yield function can be expressed in the form

$$f = 3\varepsilon_{eq}G(\theta) - \kappa_Y, \tag{14}$$

where $\kappa_Y > 0$ is a history dependent yield strain, such that the von Mises stress attains the value $\mu\kappa_Y/J_e$ when plasticity occurs, and the function

$$G(\theta) = a\,\cos\left[\frac{\arccos\left[-b\sin(3\theta)\right]}{3} - c\frac{\pi}{6}\right] > 0 \tag{15}$$

includes the material parameters a, b, and c that control the shape of the yield function in the octahedral plane.[2] Also, to be consistent with f in (14), the yield function in Panteghini and Lagioia [52] is taken to be independent of pressure.

The convexity requirement implies that the material parameters b and c must be chosen such that the yield surface is bounded, in the Haigh-Vestergaard octahedral plane, by the two extreme cases of the Galileo criterion, that are the compression cut-off and the tension cut-off (Rankine) conditions [7]. In the examples of Section 7, the von Mises and (outer) rounded Tresca criteria will also be considered. Table 1 collects the values of the material parameters for $G(\theta)$ in Eq. (15) that are needed to reproduce all the yield criteria relevant for this investigation.

[2] To account for the different sign convention for the stress tensor, which here is positive in tension, the argument of the arccos in Eq. (15) has an extra minus sign with respect to the analogous function in Lagioia and Panteghini [36], where, also, the function $G(\theta)$ is denoted as $\Gamma(\theta)$ and the parameters a, b, and c are denoted as α, β, and γ, respectively.

3. Summary of basic constitutive equations that differ between the B_e model and the LN, LN-MD models

3.1. Evolution equations for the elastic left Cauchy-Green deformation for the B_e model and for the LN, LN-MD models within a brief review of different Eulerian formulations

Eckart [12] proposed an Eulerian formulation of constitutive equations for elastic-inelastic solids and Leonov [39] proposed similar equations for polymeric media. To compare various formulations it is convenient to unify the notation. By identifying the elastic deformation tensor $\mathbf{g}$ in [12] with the symmetric positive-definite tensor $\mathbf{B}_e^{-1}$, Eqs. (20) and (21) in [12] yield the evolution equation

$$\overset{\cdot}{\overline{\mathbf{B}_e^{-1}}} = -\mathbf{B}_e^{-1}\mathbf{L} - \mathbf{L}^T\mathbf{B}_e^{-1} + J_e^{2/3}\Gamma\mathbf{B}_e^{-1}\mathbf{A}\mathbf{B}_e^{-1}, \tag{16}$$

where $\Gamma \geq 0$ is a function that controls the magnitude of the rate of inelasticity and $\mathbf{A}$ is a symmetric tensor function controlling the direction of the inelastic rate. Next, by substituting the identity

$$\overset{\cdot}{\overline{\mathbf{B}_e^{-1}}} = -\mathbf{B}_e^{-1}\dot{\mathbf{B}}_e\mathbf{B}_e^{-1}$$

into Eq. (16), one obtains the evolution equation

$$\dot{\mathbf{B}}_e = \mathbf{L}\mathbf{B}_e + \mathbf{B}_e\mathbf{L}^T - J_e^{2/3}\Gamma\mathbf{A}\,. \tag{17}$$

Furthermore, by noting the sign of the spin rate in Leonov [39] and identifying $\mathbf{c}_e$ and $\mathbf{e}_p$ there with $\mathbf{B}_e$ and the symmetric inelastic deformation rate $\mathbf{D}_p$, respectively, the evolution equation (2.4) for $\mathbf{B}_e$ in [39] can be written in the form (17) with $\mathbf{A}$ specified by

$$J_e^{2/3}\Gamma\mathbf{A} = \mathbf{D}_p\mathbf{B}_e + \mathbf{B}_e\mathbf{D}_p\,.$$

Later, by limiting attention to isotropic response, Simo [68] showed that the multiplicative formulation (1) reduces to an evolution equation for $\mathbf{B}'_e$ given by

$$\dot{\mathbf{B}}'_e = \mathbf{L}\mathbf{B}_e + \mathbf{B}_e\mathbf{L}^T - \frac{1}{3}(\mathbf{B}_e\cdot\mathbf{D})\mathbf{I} - J_e^{2/3}\Gamma\mathbf{A}'\,. \tag{18}$$

Next, by using the expressions for elastic dilatation J_e and the unimodular tensor $\bar{\mathbf{B}}_e$ (i.e., $\det(\bar{\mathbf{B}}_e) = 1$)

$$J_e^2 = \det(\mathbf{B}_e), \quad \bar{\mathbf{B}}_e = J_e^{-2/3}\mathbf{B}_e,$$

it can be shown that Eq. (17) becomes

$$\dot{\bar{\mathbf{B}}}_e + \frac{2}{3}\frac{\dot{J}_e}{J_e}\bar{\mathbf{B}}_e = \mathbf{L}\bar{\mathbf{B}}_e + \bar{\mathbf{B}}_e\mathbf{L}^T - \Gamma\mathbf{A}\,. \tag{19}$$

Moreover, since $\bar{\mathbf{B}}_e$ is unimodular, i.e.

$$\dot{\bar{\mathbf{B}}}_e\cdot\bar{\mathbf{B}}_e^{-1} = 0, \tag{20}$$

Eq. (19) yields

$$\frac{\dot{J}_e}{J_e} = \mathrm{tr}(\mathbf{D}) - \frac{1}{2}\Gamma\mathbf{A}\cdot\bar{\mathbf{B}}_e^{-1}, \tag{21}$$

so that inelasticity is isochoric, i.e.

$$\frac{\dot{J}_e}{J_e} = \mathrm{tr}(\mathbf{D}), \tag{22}$$

if $\mathbf{A}$ satisfies the restriction

$$\mathbf{A}\cdot\bar{\mathbf{B}}_e^{-1} = 0, \tag{23}$$

which is consistent with the proposal of Simo and Miehe [73], who developed an expression for $\mathbf{A}$ by resorting to the principle of maximum dissipation for isotropic materials and focusing on von Mises plasticity. In this way and under these conditions, the proposal in [68,73] removes the arbitrariness inherent the multiplicative form (1).

By following the work of Simo and Miehe [73], equations (14.44) and (14.45) in de Souza Neto et al. [11] yield an evolution equation of the form (17) with $\mathbf{A}$ specified by

$$J_e^{2/3}\Gamma\mathbf{A} = 2\dot{\gamma}\frac{\partial\Psi}{\partial\boldsymbol{\tau}}\mathbf{B}_e, \tag{24}$$

where $\dot{\gamma} > 0$ is the plastic multiplier and the derivative of the generic isotropic yield function Ψ with respect to the Kirchhoff stress $\boldsymbol{\tau}$ contributes to controlling the direction of inelastic rate. Importantly, this is the framework for the numerical algorithms recorded in Boxes 14.3 and 14.4 of de Souza Neto et al. [11], which summarize the basis of the LN and LN-MD models studied in this work. The relation between the rates Γ and $\dot{\gamma}$ will be exemplified with Eq. (57) in Section 5.

Eq. (22) can then be used to deduce that Eq. (19) can be written as

$$\dot{\bar{\mathbf{B}}}_e = \mathbf{L}'\bar{\mathbf{B}}_e + \bar{\mathbf{B}}_e\mathbf{L}'^T - \Gamma\mathbf{A}\,. \tag{25}$$

As in Rubin and Attia [63], $\mathbf{A}$ in Eq. (25) is specified in this paper by $\mathbf{A}_p$ in Eqs. (26) and (41). With respect to the formulation in Simo and Miehe [73], this simplifies the algorithm for integrating $\bar{\mathbf{B}}_e$, while still satisfying the material dissipation restriction in Eq. (31). It is remarked that different definitions of $\mathbf{A}$ yield different Eulerian evolution equations for $\bar{\mathbf{B}}_e$ and hence different $\bar{\mathbf{B}}_e$ fields.

Note that the evolution Eqs. (17) and (25) ensure that $\mathbf{B}_e$ and $\bar{\mathbf{B}}_e$, respectively, are invariant under superposed rigid body motions, because of the presence in those equations of $\mathbf{L}$ and $\mathbf{L}'$, respectively, and for the properties of the tensor $\mathbf{A}$.

3.2. Summary of the basic equations for the B_e model

3.2.1. Elastic distortional deformation

The elastic distortional deformation $\bar{\mathbf{B}}_e$ is determined as in Eq. (25) with $\mathbf{A} = \mathbf{A}_p$, i.e.

$$\dot{\bar{\mathbf{B}}}_e = \mathbf{L}'\bar{\mathbf{B}}_e + \bar{\mathbf{B}}_e\mathbf{L}'^T - \Gamma\mathbf{A}_p, \quad \mathbf{A}_p \cdot \bar{\mathbf{B}}_e^{-1} = 0\,. \tag{26}$$

Since $\bar{\mathbf{B}}_e$ is a symmetric and unimodular tensor, it has only two non-trivial independent invariants which can be specified by

$$\beta_1 = \mathrm{tr}\big(\bar{\mathbf{B}}_e\big), \quad \beta_2 = |\bar{\mathbf{B}}_e|^2\,. \tag{27}$$

Moreover, for later reference it is noted that β_1 and $\bar{\mathbf{B}}'_e$ satisfiy the equations

$$\dot{\beta}_1 = 2\bar{\mathbf{B}}'_e \cdot \mathbf{D} - \Gamma\mathrm{tr}(\mathbf{A}_p), \tag{28}$$

$$\dot{\bar{\mathbf{B}}}'_e = \mathbf{L}'\bar{\mathbf{B}}_e + \bar{\mathbf{B}}_e\mathbf{L}'^T - \frac{2}{3}\big(\bar{\mathbf{B}}'_e \cdot \mathbf{D}\big)\mathbf{I} - \Gamma\mathbf{A}'_p\,. \tag{29}$$

3.2.2. Strain energy function, rate of material dissipation, and the constitutive equation for stress

For general elastically isotropic response the specific (per unit mass) strain-energy function Σ is a general function of the invariants $\{J_e, \beta_1, \beta_2\}$. However, to obtain the simple form in Eq. (2), Σ is specified by

$$\rho_z\Sigma = K\big[J_e - 1 - \ln(J_e)\big] + \frac{1}{2}\mu(\beta_1 - 3)\,. \tag{30}$$

Note that, in the context of finite-deformation elastocplasticity, the Neo-Hookean contribution in Eq. (30), governing the change of shape, has been proposed also in [68,73].

Also, the rate of material dissipation $\mathcal{D}$ is given by

$$\mathcal{D} = \mathbf{T} \cdot \mathbf{D} - \rho\dot{\Sigma} \geq 0\,. \tag{31}$$

For the strain energy function in Eq. (30), the Cauchy stress $\mathbf{T}$ is specified by

$$\mathbf{T} = -p\mathbf{I} + \mathbf{T}', \quad p = K(J_e^{-1} - 1), \quad \mathbf{T}' = J_e^{-1}\mu\bar{\mathbf{B}}'_e = 2J_e^{-1}\mu\epsilon'_e, \tag{32}$$

where the pressure p is positive in compression. By using Eq. (9), it is easy to see that this constitutive equation is consistent with the constitutive equation in Eqs. (2) and (3) for the Kirchhoff stress.

Then, with the help of Eqs. (7), (8), and (28) the tensor $\mathbf{A}_p$ is restricted to ensure that the dissipation (31) is satisfied

$$\mathrm{tr}(\mathbf{A}_p) \geq 0 \Rightarrow \mathcal{D} = \frac{1}{2}J_e^{-1}\mu\Gamma\mathrm{tr}(\mathbf{A}_p) \geq 0\,. \tag{33}$$

3.3. Summary of the basic equations for the LN and LN-MD models

3.3.1. Elastic deformation

For the LN and LN-MD models, the elastic deformation is determined by using the definition for $\mathbf{A}$ in Eq. (24) into the evolution Eq. (17), i.e.

$$\dot{\mathbf{B}}_e = \mathbf{L}\mathbf{B}_e + \mathbf{B}_e\mathbf{L}^T - 2\dot{\gamma}\frac{\partial\Psi}{\partial\boldsymbol{\tau}}\mathbf{B}_e, \tag{34}$$

with $\Psi = \mu f$, where f is given in Eq. (14), such as

$$\Psi = \sqrt{\frac{3}{2}}|\boldsymbol{\tau}'|G(\theta) - \mu\kappa_Y$$

and the Lode angle is the function of the Kirchhoff stress as in Eq. (13).

3.3.2. Logarithmic strain, strain energy function, and constitutive equation for the stress

As stated in the Introduction, the HYPO, LN, and LN-MD models assume constitutive equations based on the logarithm of a symmetric positive-definite second-order tensor. Specifically, the HYPO model connects an objective stress rate to the rate of deformation tensor $\mathbf{D}$. In Abaqus [10], the increment of $\mathbf{D}$, which is split into its elastic and plastic parts to determine the Cauchy stress increment, is computed as the logarithm of the increment of the left stretch tensor. Instead, the LN, LN-MD models employ constitutive equations based on the logarithmic strain [19]. Therefore, the constitutive equations of these models are different from those of the B_e model, which does not rely on any logarithmic strain.

Hencky's logarithmic strain $\mathbf{E}_e$ is defined as

$$\mathbf{E}_e = \frac{1}{2}\ln(\mathbf{B}_e) = \frac{1}{3}\ln(J_e)\mathbf{I} + \mathbf{E}'_e, \quad J_e = \sqrt{\det(\mathbf{B}_e)} = \det(\mathbf{F}), \quad \mathbf{E}'_e = \frac{1}{2}\ln(\bar{\mathbf{B}}_e), \tag{35}$$

where $\mathrm{tr}(\mathbf{E}_e)$ is a pure measure of elastic dilatation and $\mathbf{E}'_e$ is a pure measure of elastic distortional deformation. It is emphasized that, although the same symbol is used to denote the deformation $\mathbf{B}_e$ for the models B_e, Ln, and Ln-MD, the field $\mathbf{B}_e$ differs for each of these models because each model adopts different evolution equations (see section 3.1).

Also, for the Ln and Ln-MD models, this investigation considers the quadratic strain energy function

$$\rho_z\Sigma = \frac{1}{2}K\,\mathrm{tr}(\mathbf{E}_e)^2 + \mu|\mathbf{E}'_e|^2, \tag{36}$$

which yields the Kirchhoff stress

$$\boldsymbol{\tau} = K\,\mathrm{tr}(\mathbf{E}_e)\mathbf{I} + 2\mu\mathbf{E}'_e, \tag{37}$$

that has the same form as (2). For more details on the Ln model the reader is referred to [11], Chapter 14.

3.4. A brief note on the choice of the elastic strain for finite-deformation elastoplasticity

For the purposes of the following discussion, it is sufficient to compare the B_e and Ln models. The Ln-MD infact, employs the same elastic strain measure and stress expression as Ln but is based on an approximate, yet accurate, derivative of the logarithmic strain.

Both the elastic strain $\mathbf{E}_e$ of the Ln model and the elastic strain $\boldsymbol{\varepsilon}_e$ of the B_e model separate the physical notions of elastic dilatation J_e and distortional deformation $\bar{\mathbf{B}}_e$. For the Ln model, both the trace and the deviatoric part of $\mathbf{E}_e$ depend nonlinearly on J_e and $\bar{\mathbf{B}}_e$, respectively. In contrast, in the B_e model, the trace of $\boldsymbol{\varepsilon}_e$ depends linearly on J_e, and its deviatoric part depends linearly on $\bar{\mathbf{B}}_e$. Consequently, the B_e model is simpler than the Ln model, as it avoids the need for a spectral decomposition of $\mathbf{B}_e$ and the associated numerical challenges of differentiating the logarithm of a tensor – an operation required, for instance, in computing the consistent tangent in finite element implementations.

It is important to note that, under isochoric plane-strain conditions, the Ln model always predicts a zero out-of-plane elastic strain component, which constrains the Lode angle (defined in terms of the deviatoric elastic strain) to be zero.

While both models can be formulated in terms of an Eulerian evolution equation for $\bar{\mathbf{B}}_e$, they involve distinct definitions of the symmetric tensor $\mathbf{A}$, which describes the directions of the rate of inelasticity. This leads to different predictions for the distortional elastic stretches.

The Kirchhoff stress $\boldsymbol{\tau}$ has the same functional form in both the Ln and B_e models, depending linearly on the elastic strains $\mathbf{E}_e$ and $\boldsymbol{\varepsilon}_e$, respectively. This similarity enables the use of numerical algorithms originally developed for small-deformation problems – such as return-mapping schemes – to solve the large-deformation equations in both models (e.g., [11] for the Ln model). However, because the strain measures differ, the resulting stress $\boldsymbol{\tau}$ generally differs between the two models, even for the same $\mathbf{B}_e$, i.e., for the same elastic stretches.

4. A Lode angle-dependent yield function for the B_e model

4.1. A direction of the plastic rate consistent with dependence on Lode angle

The tensor $\mathbf{A}_p$ that controls the direction of the plastic deformation rate has been specified in the form Rubin and Attia [63]

$$\mathbf{A}_p = \bar{\mathbf{B}}_e - \frac{3}{\mathrm{tr}\big(\bar{\mathbf{B}}_e^{-1}\big)}\mathbf{I}, \quad \mathbf{A}'_p = \bar{\mathbf{B}}'_e, \tag{38}$$

which is independent of the Lode angle. The objective of this section is to present a finite-deformation formulation, motivated by Panteghini and Lagioia [52], accounting for dependence on the Lode angle. To this purpose, it is convenient to express $\bar{\mathbf{B}}'_e$ in its spectral form

$$\begin{aligned} &\bar{\mathbf{B}}'_e = |\bar{\mathbf{B}}'_e|\mathbf{U}', \quad |\mathbf{U}'| = 1, \\ &\mathbf{U}' = \sqrt{\frac{2}{3}}\Big[\cos\Big(\frac{\pi}{6}+\theta\Big)\mathbf{p}_1\otimes\mathbf{p}_1 + \sin(\theta)\mathbf{p}_2\otimes\mathbf{p}_2 - \cos\Big(\frac{\pi}{6}-\theta\Big)\mathbf{p}_3\otimes\mathbf{p}_3\Big], \end{aligned} \tag{39}$$

where $\mathbf{p}_i$ is the ordered orthonormal triad of eigenvectors of $\bar{\mathbf{B}}'_e$ with $\mathbf{p}_1$ associated with the largest eigenvalue and $\mathbf{p}_3$ associated with the smallest eigenvalue. Also, $\mathbf{U}'$ is the unit deviatoric tensor defining the direction of $\bar{\mathbf{B}}'_e$. Using this representation, the unit deviatoric tensor $\mathbf{N}'$ normal to $\mathbf{U}'$, defined by the increasing direction of θ, is given by

$$\begin{aligned} &\mathbf{N}' = \frac{\partial\mathbf{U}'}{\partial\theta} = \sqrt{\frac{2}{3}}\Big[-\sin\Big(\frac{\pi}{6}+\theta\Big)\mathbf{p}_1\otimes\mathbf{p}_1 + \cos(\theta)\mathbf{p}_2\otimes\mathbf{p}_2 - \sin\Big(\frac{\pi}{6}-\theta\Big)\mathbf{p}_3\otimes\mathbf{p}_3\Big], \\ &|\mathbf{N}'| = 1, \quad \mathbf{N}'\cdot\mathbf{U}' = 0\,. \end{aligned} \tag{40}$$

Now, motivated by the direction of the rate of small-deformation plastic strain in Panteghini and Lagioia [52], the tensor $\mathbf{A}_p$ in Eq. (38) for the finite-deformation formulation is generalized to take the form

$$\mathbf{A}_p = \bar{\mathbf{B}}_e + \eta|\bar{\mathbf{B}}'_e|\mathbf{N}' - \frac{3+\eta|\bar{\mathbf{B}}'_e|\,\mathbf{N}'\cdot\bar{\mathbf{B}}_e^{-1}}{\mathrm{tr}(\bar{\mathbf{B}}_e^{-1})}\mathbf{I}, \quad \eta = \frac{G'}{G}, \quad G' \equiv \frac{\mathrm{d}G}{\mathrm{d}\theta}, \tag{41}$$

where η (which, notably, is independent of the material parameter a) introduces dependence on the Lode angle and the restriction (26) on $\mathbf{A}_p$, that ensures $\bar{\mathbf{B}}_e$ to remain unimodular, is satisfied. Note that the parameter η vanishes when the yield function is independent of θ, consistently with the particularization of Eq. (41) to Eq. (38). Next, substituting Eq. (41) into Eq. (29) and using Eq. (3) yields

$$\begin{aligned}
&\dot{\boldsymbol{\epsilon}}'_e = \frac{1}{2}\dot{\bar{\mathbf{B}}}'_e = \frac{1}{2}\left[\mathbf{L}'\bar{\mathbf{B}}_e + \bar{\mathbf{B}}_e\mathbf{L}'^T - \frac{2}{3}(\bar{\mathbf{B}}'_e\cdot\mathbf{D})\mathbf{I}\right] - \mathbf{D}'_p,\\
&\mathbf{D}'_p = \frac{1}{2}\Gamma\mathbf{A}'_p = \Gamma|\boldsymbol{\epsilon}'_e|(\mathbf{U}' + \eta\mathbf{N}'), \quad \mathrm{tr}(\mathbf{D}_p) \equiv 0,
\end{aligned} \tag{42}$$

where $\mathbf{D}'_p$ is defined as the plastic deformation rate. It can be shown that $\mathbf{D}'_p$ is normal to the yield surface $f = 0$ in Eq. (14), which is consistent with the small-deformation model in Panteghini and Lagioia [52] when the yield function there is independent of pressure. It therefore follows that the proposed formulation is consistent with a small-deformation associated flow rule with respect to ε_{eq}, θ. Moreover, it is emphasized that the evolution Eq. (42) is fully nonlinear. Also, it is noted that the restriction given by Eq. (33) for non-negative rate of material dissipation is different from the small-deformation restriction $\boldsymbol{\tau}'\cdot\mathbf{D}'_p \geq 0$ because of the dependence of the strain-energy function in Eq. (30) on β_1.

4.1.1. Analysis of the direction of plastic rate in Tresca plasticity

The exact Tresca yield function can be obtained by using (15) with the specifications

$$a = \frac{1}{\sin(\frac{\pi}{3})}, \quad b = 1, \quad c = 1, \tag{43}$$

and, with the help of Eqs. (39), (40), and (42), to obtain

$$G = \cos(\theta), \quad \eta = -\tan(\theta), \quad \mathbf{D}'_p\cdot(\mathbf{p}_2\otimes\mathbf{p}_2) = 0, \tag{44}$$

where η is specified by (41). Then, by using this result, it follows that

$$\begin{aligned}
&\mathbf{D}'_p = \Gamma|\boldsymbol{\epsilon}'_e|\sec(\theta)(\mathbf{p}_1\otimes\mathbf{p}_1 - \mathbf{p}_3\otimes\mathbf{p}_3) = \Gamma|\boldsymbol{\epsilon}'_e|\sec(\theta)(\mathbf{a}_1\otimes\mathbf{a}_3 + \mathbf{a}_3\otimes\mathbf{a}_1),\\
&\mathbf{a}_1 = \frac{1}{\sqrt{2}}(\mathbf{p}_1 + \mathbf{p}_3), \quad \mathbf{a}_3 = \frac{1}{\sqrt{2}}(\mathbf{p}_1 - \mathbf{p}_3),
\end{aligned} \tag{45}$$

which corresponds to plastic simple shearing rate in the $\mathbf{a}_1\otimes\mathbf{a}_3$ direction with no component normal to this plane.

The foregoing distinctive feature of Tresca plasticity holds for all the finite-deformation models analyzed here and becomes evident when observing that the plastic potential is an isotropic function of the Kirchhoff stress $\boldsymbol{\tau}$, which is independent of the intermediate principal component of $\boldsymbol{\tau}$. Consequently, since for all these models the direction of the plastic deformation rate $\mathbf{D}'_p$ coincides with the derivative of the plastic potential with respect to $\boldsymbol{\tau}$, the plastic deformation rate $\mathbf{D}'_p$ has no component along the intermediate principal direction of $\boldsymbol{\tau}'$ [35].

4.2. Hardening

Often, the hardening parameter is expressed as a function $\kappa_Y(\varepsilon_p)$ of the equivalent plastic strain ε_p. Using the definition of $\mathbf{D}'_p$ in Eq. (42), ε_p is determined by integrating the evolution equation

$$\dot{\varepsilon}_p = \sqrt{2/3}|\mathbf{D}'_p| = \Gamma\varepsilon_{eq}\sqrt{1+\eta^2}\,. \tag{46}$$

In general, a plastic strain tensor is not an internal state variable in the sense of Onat [47] since it typically depends on the choice of the reference configuration from which it is measured. In contrast, the value of κ_Y is an internal state variable since its value can be determined by measuring the yield stress in the current configuration, independent of a choice of a reference configuration. Consequently, since ε_p is a monotonically increasing function of loading, its value can be determined by measuring the value of κ_Y and its rate $\dot{\kappa}_Y$ even when $\kappa_Y(\varepsilon_p)$ models softening as long as the softening is monotonic.

4.3. Dissipation

Using the modified form of $\mathbf{A}_p$ in Eq. (41) the dissipation given in Eq. (33) requires

$$\mathrm{tr}(\mathbf{A}_p) = \frac{1}{\mathrm{tr}(\bar{\mathbf{B}}_e^{-1})}\left[\mathrm{tr}(\bar{\mathbf{B}}_e)\mathrm{tr}(\bar{\mathbf{B}}_e^{-1}) - 9 - 3\eta|\bar{\mathbf{B}}'_e|(\mathbf{N}'\cdot\bar{\mathbf{B}}_e^{-1})\right] \geq 0, \tag{47}$$

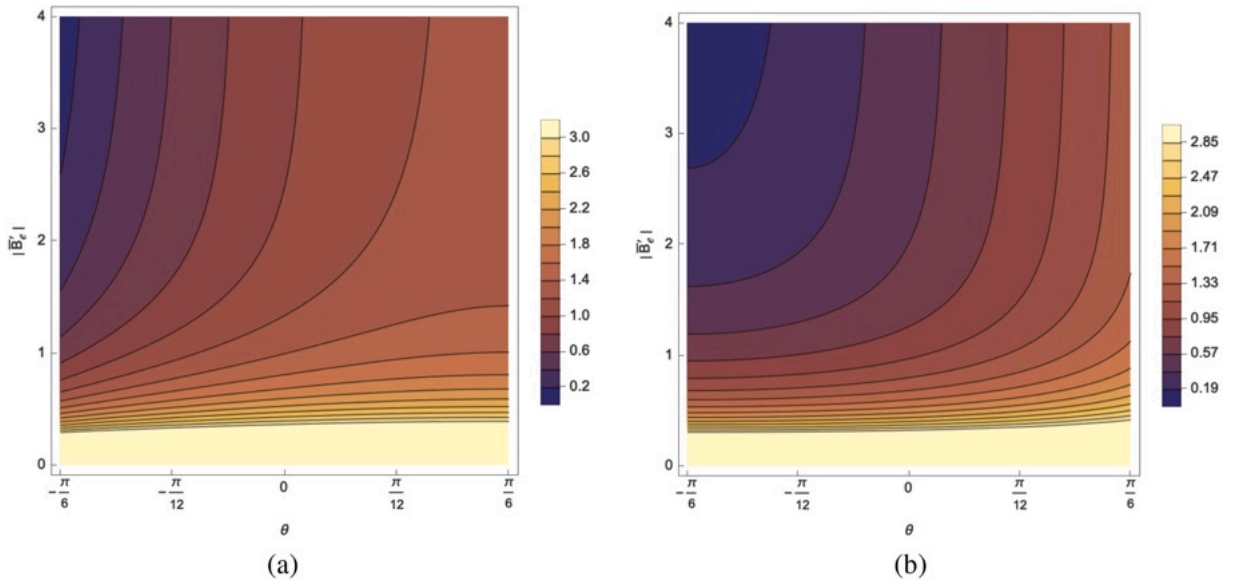

Fig. 1. Contours of the function $A = A_1 + A_2$ in Eq. (48), whose positiveness ensures non-negative dissipation, for the two extreme cases of the Galileo criterion: (a) compression cut-off and (b) tension cut-off (Rankine), as defined in Table 1.

which, with the help of Eqs. (A.1) and (A.2), can be written in the form

$$\begin{aligned} &\mathrm{tr}(\mathbf{A}_p) = \frac{3|\bar{\mathbf{B}}'_e|^3 A}{\mathrm{tr}\left(\bar{\mathbf{B}}_e^{-1}\right)} \geq 0, \quad A = A_1 + A_2, \\ &A_1 = \frac{\beta_1}{3|\bar{\mathbf{B}}'_e|}, \quad A_2 = \frac{1}{\sqrt{6}}\left[\sin(3\theta) + \eta\cos(3\theta)\right]. \end{aligned} \tag{48}$$

From the solutions for β_1 in Eq. (A.6) it can be shown that $A_1 \geq 1/\sqrt{6}$. Moreover, the bounding yield surfaces are the compression cut-off and the tension cut-off (Rankine) criteria.

For the compression cut-off (Table 1),

$$A_2 = [\sin(3\theta) + \cot(\theta + \pi/3)\cos(3\theta)]/\sqrt{6},$$

while, for the tension cut-off (Rankine) (Table 1),

$$A_2 = [\sin(3\theta) - \tan(\theta + \pi/6)\cos(3\theta)]/\sqrt{6}.$$

Both these functions are monotonic functions of $\theta \in [-\pi/6, \pi/6]$ and both of them attain the same minimum $-1/\sqrt{6}$ at $\theta = -\pi/6$. Consequently, $A \geq 0$ and the rate of material dissipation is non-negative for all solutions. Additionally, Fig. 1 displays contours of the values assumed by A in Eq. (48) as a function of $\theta \in [-\pi/6, \pi/6]$ and $|\bar{\mathbf{B}}'_e| \in [0, 4]$ for the two extreme cases of Galileo's criterion, that are the compression cut-off and the tension cut-off (Rankine).

5. Integration algorithm for the constitutive equations

5.1. Basics and elastic dilatation

Consider a time step from $t = t_n$ to $t = t_{n+1} = t_n + \Delta t$. A generic field g is denoted as $g(t_n)$ at the beginning of the time step and simply as g at the end of the time step, with $\Delta g = g - g(t_n)$ and $\Delta g/\Delta t$ its increment and its rate in the time step.

Following Simo [70], it is recalled that the relative deformation gradient $\mathbf{F}_r$, the relative dilatation J_r, and the unimodular relative distortional deformation gradient $\bar{\mathbf{F}}_r$ from the beginning of the time step satisfy the equations

$$\begin{aligned} &\dot{\mathbf{F}}_r = \mathbf{L}\mathbf{F}_r, \qquad \mathbf{F}_r(t_n) = \mathbf{I}, \\ &J_r = \det(\mathbf{F}_r), \qquad \frac{\dot{J}_r}{J_r} = \mathrm{tr}(\mathbf{D}), \quad J_r(t_n) = 1, \\ &\bar{\mathbf{F}}_r = J_r^{-1/3}\mathbf{F}_r, \quad \dot{\bar{\mathbf{F}}}_r = \mathbf{L}'\bar{\mathbf{F}}_r, \quad \bar{\mathbf{F}}_r(t_n) = \mathbf{I}. \end{aligned} \tag{49}$$

This relative deformation gradient $\mathbf{F}_r$ can be determined directly by the displacement increments during the time step. Alternatively, $\mathbf{F}_r$ can be expressed in terms of the total deformation gradient $\mathbf{F}$ by the expression

$$\mathbf{F}_r = \mathbf{F}\mathbf{F}^{-1}(t_n). \tag{50}$$

Using these expressions, the exact solution of the evolution Eq. (7) for J_e is given by

$$J_e = J_r J_e(t_n)\,. \tag{51}$$

Since plastic dilatation is ignored and $J_e = 1$ in the initial configuration in which $\mathbf{F} = \mathbf{I}$, it follows that $J_e = \det(\mathbf{F})$.

5.2. Algorithms for elastic distortional deformation and hardening

Since all B_e, LN, and LN-MD models share the common feature that the plastic deformation rate is normal to the yield surface, for all of them any small-deformation algorithm to determine the elastic distortional deformation and the hardening can be adopted by writing the selected algorithm in terms of the Kirchhoff stress, see Eqs. (2) and (9)–(12).

Here, the small-deformation algorithm proposed in Panteghini and Lagioia [52], which is return algorithm in the invariants stress space, is adopted. One of the main issues that this algorithm addresses is concerned with the case in which two stress eigenvalues are repeated, for which the derivative of the Lode angle with respect to the stress tensor is undefined.

Isotropy allows the formulation of an implicit integration algorithm in terms of the invariants

$$\varepsilon^*_{eq} = \sqrt{2/3}|\boldsymbol{\mathcal{E}}^{*\prime}|, \quad \theta^* = -\frac{1}{3}\sin^{-1}\frac{27\det(\boldsymbol{\mathcal{E}}^{*\prime})}{2\gamma^{*3}_e}, \quad -\frac{\pi}{6} \le \theta^* \le \frac{\pi}{6}, \quad \gamma^*_e = 3\varepsilon^*_{eq}/2,$$

which denote the equivalent elastic distortional strain and the Lode angle associated with the generic *elastic* strain predictor

$$\boldsymbol{\mathcal{E}}^* = \boldsymbol{\mathcal{E}}(t_n) + \Delta\boldsymbol{\mathcal{E}}^*,$$

where $\Delta\boldsymbol{\mathcal{E}}^*$ is the increment of $\boldsymbol{\mathcal{E}}$ if no plasticity occurs in the increment. The specific form of the predictor $\boldsymbol{\mathcal{E}}^*$ has to be selected depending on adopted finite-deformation model.

The equivalent von Mises stress predictor q^* associated to the Kirchhoff stress $\boldsymbol{\tau}$ simply reads

$$q^* = 3\mu\,\varepsilon^*_{eq}, \quad q^* = J_e\sigma^*_e\,. \tag{52}$$

By using the yield function in Eq. (14), if

$$\mu f^* \equiv q^* G(\theta^*) - \mu\kappa_Y(t_n) \le 0, \tag{53}$$

the response is elastic and the Kirchhoff stress τ follows Eq. (2), namely

$$\tau = K\mathrm{tr}(\boldsymbol{\mathcal{E}}^*)\mathbf{I} + 2\mu\boldsymbol{\mathcal{E}}^{*\prime}\,.$$

Otherwise, if $f^* > 0$, the predictor solution must be discarded. By assuming an implicit integration scheme, trigonometric manipulations in the Haigh-Westergaard space yield [52]

$$\Delta\varepsilon^p_q = \varepsilon^*_{eq}\cos(\theta^* - \theta) - \varepsilon_{eq}, \quad \Delta\varepsilon^p_\theta = \varepsilon^*_{eq}\sin(\theta^* - \theta), \tag{54}$$

where, in the Haigh-Westergaard plane with polar coordinates (q, θ), $\Delta\varepsilon^p_q$ and $\Delta\varepsilon^p_\theta$ are the plastic strain increments along the radial and tangential directions, respectively, and θ and ε_{eq} are the unkown values at the end of the increment.

The same quantities in Eq. (54) can be computed by resorting to the normality rule, i.e.

$$\Delta\varepsilon^p_q = \mu\frac{\partial f}{\partial q}\Delta\gamma = G(\theta)\Delta\gamma, \quad \Delta\varepsilon^p_\theta = \frac{\mu}{q}\frac{\partial f}{\partial\theta}\Delta\gamma = G'(\theta)\Delta\gamma, \tag{55}$$

where $\Delta\gamma > 0$ is the plastic multiplier increment. Below, $\dot\gamma$ will be related to Γ in Eq. (26) for use of this algorithm in the B_e model.

5.2.1. The case $G'(\theta^*) = 0$

From the second relation in Eq. (55), if $G'(\theta) = 0$ it results $\Delta\varepsilon^p_\theta = 0$, such that $\theta = \theta^*$ from the second relation in Eq. (54). Hence, when $G'(\theta^*) = 0$, the plastic strain increment has vanishing component in θ direction, and the assumed Backward Euler rule becomes coincident with a simple radial return. Notably, this feature allows for conveniently handling the case of two repeated eigenvalues. In this case ($G'(\theta^*) = 0$)

$$q = q^* - 3\mu G(\theta^*)\Delta\gamma, \tag{56}$$

where $\Delta\gamma$ can then be computed by solving the nonlinear scalar equation

$$\left[q^* - 3\mu G(\theta^*)\Delta\gamma\right] - \mu\kappa_Y = 0,$$

in which κ_Y is evaluated at the end of the step, i.e.

$$\kappa_Y = \kappa_Y(\varepsilon_p(t_n) + G(\theta^*)\Delta\gamma)$$

and $\varepsilon_p(t_n)$ is the accumulated equivalent plastic strain at the beginning of the increment,[3] with

$$\Delta\varepsilon_p = \sqrt{(\Delta\varepsilon^p_q)^2 + (\Delta\varepsilon^p_\theta)^2} = \Delta\gamma G\sqrt{1+\eta^2}\,.$$

[3] Note that the field ε_p here is denoted as $\varepsilon^p_{q\theta}$ in Panteghini and Lagioia [52].

The function Γ in the B_e model can be obtained by comparing this relation in terms of rates, i.e. $\dot{\varepsilon}_p = \dot{\gamma} G \sqrt{1+\eta^2}$, with Eq. (46) to deduce that

$$\Gamma \dot{\varepsilon}_{eq} = \dot{\gamma}\, G, \tag{57}$$

or, in terms of increments,

$$\Delta\Gamma \varepsilon_{eq} = \Delta\gamma\, G\,. \tag{58}$$

The Kirchhoff stress can then be computed as

$$\boldsymbol{\tau} = K \mathrm{tr}(\boldsymbol{\mathcal{E}}^*)\mathbf{I} + \frac{2\mu\, q}{q^*}\boldsymbol{\mathcal{E}}^{*\prime}\,.$$

5.2.2. The case $G'(\theta^*) \neq 0$

For the case $G'(\theta^*) \neq 0$, ε_{eq} can be computed as a function of the final value of the Lode angle only by combining Eqs. (54) and (55) to obtain

$$\varepsilon_{eq} = \varepsilon^*_{eq}\left[\cos(\theta^* - \theta) - \frac{\sin(\theta^* - \theta)}{\eta(\theta)}\right]. \tag{59}$$

The total equivalent plastic strain increment is equal to

$$\Delta\varepsilon_p = \varepsilon^*_{eq}\sin(\theta^* - \theta)\sqrt{1 + \frac{1}{\eta(\theta)^2}}\,.$$

Then, the final value of the Lode angle can be computed by solving the nonlinear scalar equation

$$3\varepsilon_{eq}\, G(\theta) - \kappa_Y(\varepsilon_p(t_n) + \Delta\varepsilon_p) = 0\,.$$

Once θ and $q = 3\mu\varepsilon_{eq}$ are computed, the (ordered) principal components of $\boldsymbol{\tau}$ read

$$\tau_1 = K\mathrm{tr}(\boldsymbol{\mathcal{E}}^*) + \frac{2}{3}q\sin\left(\theta + \frac{2}{3}\pi\right), \quad \tau_2 = K\mathrm{tr}(\boldsymbol{\mathcal{E}}^*) + \frac{2}{3}q\sin(\theta), \quad \tau_3 = K\mathrm{tr}(\boldsymbol{\mathcal{E}}^*) + \frac{2}{3}q\sin\left(\theta - \frac{2}{3}\pi\right).$$

The Kirchhoff stress is finally determined by resorting to the spectral theorem, observing that, due to isotropy, the eigenbasis of $\boldsymbol{\tau}$ and $\boldsymbol{\mathcal{E}}^{*\prime}$ are coincident. This yields [50]

$$\tau = \sum_{i=1}^{3} \tau_i \frac{\partial \boldsymbol{\mathcal{E}}^{*\prime}}{\partial \lambda_i^*},$$

with λ_i^* denoting the (ordered) principal components of $\boldsymbol{\mathcal{E}}^{*\prime}$.

5.2.3. Form of the elastic predictor for different finite-deformation models

As already pointed out, the foregoing algorithm can be used for the B_e, LN, and LN-MD models studied in this investigation. Specifically, in the B_e model, the elastic predictor $\boldsymbol{\mathcal{E}}^*$ is

$$\boldsymbol{\varepsilon}^*_e = \frac{J_e - 1}{3}\mathbf{I} + \frac{1}{2}\bar{\mathbf{B}}^{*\prime}_e,$$

where

$$\bar{\mathbf{B}}^{*\prime}_e = J_r^{-2/3}\mathbf{F}_r\bar{\mathbf{B}}'_e(t_n)\mathbf{F}_r{}^T\,.$$

Instead, in the LN and LN-MD models the elastic predictor $\boldsymbol{\mathcal{E}}^*$ refers to the Hencky's logarithmic strain in Eq. (35), i.e.

$$\mathbf{E}^*_e = \frac{1}{2}\ln\left(\mathbf{B}^*_e\right),$$

where

$$\mathbf{B}^*_e = \mathbf{F}_r\mathbf{B}_e(t_n)\mathbf{F}_r{}^T, \quad \mathbf{B}_e(t_n) = \exp\left[2\mathbf{E}(t_n)\right].$$

For completeness, in Appendix B the algorithm for elastic distortional deformation and hardening in the B_e model is re-derived by directly starting from the equations presented in Sections 3 and 4, also showing that it is a strongly objective algorithm, i.e. both $\bar{\mathbf{B}}^{*\prime}_e$ and $\bar{\mathbf{B}}'_e$ are properly invariant under superposed rigid body motions (e.g., Jabareen [23]).

5.2.3.1. Characteristic feature of the LN-MD model. In contrast to the LN model, the LN-MD model uses expressions for the logarithm of a symmetric positive-definite second-order tensor based on projection operators developed in Luehr and Rubin [41], Sylvester [76] and summarized in Appendix C. Additionally, the LN-MD model uses an approximate and simple, yet accurate, derivative of the logarithm of a symmetric tensor, which is provided in Appendix D, that does not need the spectral representation of symmetric second-order tensors and is shown to be valid for 3D elastoplasticity of metals with small elastic strains.

6. Finite element formulation

The purpose of this section is to review the FE formulation with necessary modifications for large deformations. The FE formulation below is as commonly implemented in user element (`uel`) subroutines for Abaqus for the LN, LN-MD, and B_e models, whose results are then discussed by using exactly the same finite elements. The HYPO model, instead, employs the finite elements available in the Abaqus library.

6.1. Computation of the residuals

The internal virtual power of a continuum occupying a region P in the current configuration is expressed as

$$\delta W_i = \int_P \mathbf{T} \cdot \delta \mathbf{D} \, \mathrm{d}V, \tag{60}$$

where the $\delta\boldsymbol{\alpha}$ is any kinematically admissible variation of the general field $\boldsymbol{\alpha}$ and $\mathrm{d}V$ is the element of volume in the current configuration.

The adopted FE discretization is isoparametric, such that the same shape functions are employed to interpolate both the reference geometry and the displacement field, i.e.

$$x_{R,j}(\mathbf{r}) = \sum_{i=1}^{n} N^{(i)}(\mathbf{r}) \hat{x}_{R,j}^{(i)}, \quad u_j(\mathbf{r}) = \sum_{i=1}^{n} N^{(i)}(\mathbf{r}) \hat{u}_j^{(i)},$$

where $x_{R,j}$ and u_j are the j-th components of the reference coordinates and of the displacement, respectively, n is the total number of nodes, $N^{(i)}(\mathbf{r})$ is a standard polynomial shape function referred to the i-th node, $\mathbf{r}$ is the vector containing the intrinsic coordinates of the parent element, and $\hat{x}_{R,j}^{(i)}$ and $\hat{u}_j^{(i)}$ are, respectively, the j-th coordinate and the j-th displacement component of the i-th node.

The derivatives of the shape functions with respect to the reference coordinate system can be computed as

$$\mathbf{H}_R = \mathbf{J}_R^{-1} \mathbf{H}_p,$$

where $\mathbf{H}_p$ is the matrix that contains the derivatives of the shape functions with respect to $\mathbf{r}$ and $\mathbf{J}_R$ is the jacobian matrix.[4]

Under these assumptions, the deformation gradient $\mathbf{F}$ at the end of a generic step, which has to be stored in an array,[5] can be computed as a function of the nodal displacements, ordered in the vector $\hat{\mathbf{u}}$, as:

$$\mathbf{F} = \mathbf{I} + \nabla_{x_R} \mathbf{u} = \mathbf{I} + \mathcal{A}(\mathbf{H}_R)\, \hat{\mathbf{u}},$$

where $\mathcal{A}(\mathbf{H}_R)$ is a linear function that maps the components of $\mathbf{H}_R$ into a $5 \times 2n$ matrix for 2D FEs, or into a $9 \times 3n$ matrix for 3D FEs.

The derivatives of the shape functions with respect to the *current* configuration can be computed as

$$\mathbf{H} = \mathbf{J}^{-1} \mathbf{H}_p, \tag{61}$$

where

$$\mathbf{J} = \mathbf{J}_R \mathbf{F}^T, \quad \mathbf{J}^{-1} = \mathbf{F}^{-T} \mathbf{J}_R^{-1}. \tag{62}$$

The rate of deformation in Eq. (6) is computed as a function of the nodal displacement rates, as

$$\mathbf{D} = \mathcal{B}(\mathbf{H})\, \dot{\hat{\mathbf{u}}},$$

[4] All the matrices and operators, for plane-strain, axisymmetric, and 3D brick elements are reported in Appendix E.

[5] At the implementation level, the nonzero components of each second-order 2D tensor (symmetric or non-symmetric) are stored in a 5-component vector. For instance,

$$[\mathbf{F}] = \begin{bmatrix} F_{11} & F_{12} & 0 \\ F_{21} & F_{22} & 0 \\ 0 & 0 & F_{33} \end{bmatrix} \rightarrow \mathbf{F} = \begin{bmatrix} F_{11} \\ F_{22} \\ F_{33} \\ F_{12} \\ F_{21} \end{bmatrix}$$

In the case of a 3D tensor, the components are stored in a 9-component vector, as

$$[\mathbf{F}] = \begin{bmatrix} F_{11} & F_{12} & F_{13} \\ F_{21} & F_{22} & F_{23} \\ F_{31} & F_{32} & F_{33} \end{bmatrix} \rightarrow \mathbf{F} = \begin{bmatrix} F_{11} \\ F_{22} \\ F_{33} \\ F_{12} \\ F_{13} \\ F_{23} \\ F_{21} \\ F_{31} \\ F_{32} \end{bmatrix}$$

where $\mathcal{B}(\mathbf{H})$ is a linear function that maps the components of the matrix $\mathbf{H}$ into a $5 \times 2n$ matrix for 2D FEs, or into a $9 \times 3n$ matrix for 3D FEs.

Hence, the internal virtual power given in Eq. (60) is discretized as

$$\delta W_i = \int_P \left[\mathcal{B}(\mathbf{H})^T \mathbf{T}\right] \delta\tilde{\mathbf{u}} \mathrm{d}V \,.$$

By observing that $\mathrm{d}V = J_e \mathrm{d}V_R$, the internal force is computed by integrating in the reference configuration P_R as

$$\mathbf{F}^{int} = \int_{P_R} \left[\mathcal{B}(\mathbf{H})^T \mathbf{T}\right] J_e \, \mathrm{d}V_R = \int_{P_R} \left[\mathcal{B}(\mathbf{H})^T \boldsymbol{\tau}\right] \mathrm{d}V_R \,. \tag{63}$$

Finally, on the basis of Section 5, the numerical procedures for evaluating the stress for the B_e model and the LN, LN-MD models are provided in Algorithms 1 and 2, respectively. For the LN model this investigation uses the coding provided in de Souza Neto et al. [11], which holds only for 2D problems, while the LN-MD model here implemented is valid also for 3D problems. de Souza Neto et al. [11] explain that, in general, the return algorithm for the LN model requires an exponential map for determining the influence of $\mathbf{F}_p$. However, this exponential map can be eliminated when logarithmic strains are adopted. For this reason, Algorithm 2 limits attention to the determination of the elastic trial value of the logarithmic strain.

Algorithm 1 Computation of the Cauchy stress $\mathbf{T}$ and of $\bar{\mathbf{B}}_e$.

Compute:

$$\mathbf{F} = \mathbf{I} + \mathcal{A}(\mathbf{H}_R)\,\hat{\mathbf{u}}, \quad \mathbf{F}_n = \mathbf{I} + \mathcal{A}(\mathbf{H}_R)\,\hat{\mathbf{u}}_n$$

Compute:

$$\mathbf{F}_r = \mathbf{F}\,\mathbf{F}_n^{-1}, \quad J_r = J_e / J_e(t_n),$$

Compute the unimodular predictor:

$$\bar{\mathbf{B}}_e^{*\prime} = J_r^{-2/3} \mathbf{F}_r \bar{\mathbf{B}}_e'(t_n) \mathbf{F}_r{}^T$$

Compute the elastic strain predictor:

$$\boldsymbol{\varepsilon}_e^* = \frac{J_e - 1}{3}\mathbf{I} + \frac{1}{2}\bar{\mathbf{B}}_e^{*\prime}$$

Call the small strain plasticity routine $\rightarrow \boldsymbol{\tau}(\boldsymbol{\varepsilon}_e^*)$ and $\partial\boldsymbol{\tau}/\partial\boldsymbol{\varepsilon}_e^*$
Compute the Cauchy stress tensor:

$$\mathbf{T} = J_e^{-1}\boldsymbol{\tau}$$

Compute the consistent tangent operator:

$$\partial\mathbf{T}/\partial\mathbf{F} = \partial\boldsymbol{\tau}/\partial\boldsymbol{\varepsilon}_e^* \left(\frac{1}{2\det\mathbf{F}} \partial\bar{\mathbf{B}}_e^{*\prime}/\partial\mathbf{F} + \frac{1}{3}\mathbf{I}\otimes\mathbf{F}^{-T} \right) - \mathbf{T}\otimes\mathbf{F}^{-T}$$

where $\partial\bar{\mathbf{B}}_e^{*\prime}/\partial\mathbf{F}$ is given in Eq. (F.1) of Appendix F.
Compute the deviatoric elastic strain:

$$\bar{\mathbf{B}}_e' = \boldsymbol{\tau}'/\mu$$

Compute $\bar{\mathbf{B}}_e$ using (A.4) and (A.6)

6.2. FE stiffness matrix

The FE stiffness matrix is obtained by differentiating the internal forces $\mathbf{F}^{int}$ with respect to the nodal displacements $\hat{\mathbf{u}}$. Observing that $\mathcal{B}(\mathbf{H})$ is a function of the derivatives of the shape functions in the current configuration, the computation of the FE stiffness matrix requires differentiation with respect to the nodal displacements. Combining Eq. (61) and (62) yields

$$\mathbf{H} = \mathbf{F}^{-T}\mathbf{J}_R^{-1}\mathbf{H}_p,$$

Hence:

$$\partial\mathbf{H}/\partial\mathbf{F}_j = \left(\partial\mathbf{F}^{-1}/\partial\mathbf{F}_j\right)^T \mathbf{J}_R^{-1}\mathbf{H}_p,$$

where[6]

$$\frac{\partial\left(\mathbf{F}^{-1}\right)_{ij}}{\partial(\mathbf{F})_{hk}} = -\left(\mathbf{F}^{-1}\right)_{ih}\left(\mathbf{F}^{-1}\right)_{kj} \,. \tag{64}$$

[6] The derivative in Eq. (64) must be properly mapped in array notation to compute $\partial(\mathbf{F}^{-1})_I/\partial\mathbf{F}_m$.

Algorithm 2 Algorithm for F_eF_p plasticity (from Box 14.3 in de Souza Neto et al. [11]).

Compute:

$$\mathbf{F} = \mathbf{I} + \mathcal{A}(\mathbf{H}_R)\,\hat{\mathbf{u}}, \quad \mathbf{F}_n = \mathbf{I} + \mathcal{A}(\mathbf{H}_R)\,\hat{\mathbf{u}}_n$$

Compute:

$$\mathbf{F}_r = \mathbf{F}\,\mathbf{F}_n^{-1}$$

Compute the elastic trial state:

$$\mathbf{B}_e(t_n) = \exp\left[2\mathbf{E}(t_n)\right]$$

$$\mathbf{B}_e^* = \mathbf{F}_r\mathbf{B}_e(t_n)\mathbf{F}_r{}^T$$

Compute the elastic strain predictor:

$$\mathbf{E}_e^* = \frac{1}{2}\ln\left(\mathbf{B}_e^*\right)$$

Call the small strain plasticity routine $\rightarrow \boldsymbol{\tau}(\mathbf{E}_e^*)$, $\mathbf{E}_e$ and $\partial\boldsymbol{\tau}/\partial\mathbf{E}_e^*$

Compute the Cauchy stress tensor:

$$\mathbf{T} = J_e^{-1}\boldsymbol{\tau}$$

Compute the consistent tangent operator:

$$\partial\mathbf{T}/\partial\mathbf{F} = \partial\boldsymbol{\tau}/\partial\mathbf{E}_e^*\left(\frac{1}{\det\mathbf{F}}\partial\mathbf{E}_e^*/\partial\mathbf{B}_e^*\right)\partial\mathbf{B}_e^*/\partial\mathbf{F} - \mathbf{T}\otimes\mathbf{F}^{-T}$$

where $\partial\mathbf{B}_e^*/\partial\mathbf{F}$ is given in Eq. (F.2)

Since $\mathcal{B}(\mathbf{H})$ is a linear operator, it follows that

$$\partial\mathcal{B}(\mathbf{H})/\partial\mathbf{F}_j = \mathcal{B}(\partial\mathbf{H}/\partial\mathbf{F}_j)\,.$$

Finally, computing the derivative of Eq. (63) yields

$$\partial\mathbf{F}^{int}/\partial\hat{\mathbf{u}} = \int_{P_0}\left\{\left[\mathcal{B}(\mathbf{H})^T\left(\partial\mathbf{T}/\partial\mathbf{F} + \mathbf{T}\otimes\mathbf{F}^{-T}\right) + \mathbf{B}_T\right]\mathcal{A}(\mathbf{H}_R)\right\}J_e\mathrm{d}V_R,$$

where

$$\left(\mathbf{B}_T\right)_j = \mathcal{B}\left(\partial\mathbf{H}/\partial\mathbf{F}_j\right)^T\mathbf{T}\,.$$

7. Assessment through benchmak problems involving large deformations

The following examples compare predictions and computational costs using the built-in hypoelastic constitutive option in Abaqus, here denoted as HYPO model, and the hyperelastic models LN, LN-MD, and B_e, previously presented. Since the material library of Abaqus does not include the Tresca criterion, all the models use the rounded Tresca yield function developed in Lagioia and Panteghini [36] with a rounding parameter $b = 0.9999$ (see Table 1). Specifically, for the HYPO model such criterion is implemented in a user material subroutine (`umat`) for Abaqus, as developed in Panteghini and Lagioia [52].

The considered benchmark problems are the plane-strain cyclic shearing of a square block, presented in Section 7.2, the necking of a circular cylindrical bar as in de Souza Neto et al. [11], which is presented in Section 7.3, and the drawing of a bar with a rectangular cross-section as in Panteghini [49], which is presented in Section 7.4. The assessment, however, begins in Section 7.1 with an analysis of the elastic strain measures used in the models under investigation.

Note that some figures are plotted as functions of time, but since all models are rate-independent, the rate of loading does not influence the results.

7.1. Preliminary analysis of the elastic strains adopted by the B_e and LN, LN-MD models

To start analyzing differences in the constitutive equations between the B_e model and of the LN, LN-MD models, it is convenient to compare the strain $\boldsymbol{\varepsilon}_e$ in Eq. (3) with the logarithmic strain $\mathbf{E}_e$ in Eq. (35).

To this purpose, first the volumetric strains are written as functions of J_e in the forms

$$\varepsilon_v = \mathrm{tr}(\boldsymbol{\varepsilon}_e) = J_e - 1, \quad E_v = \mathrm{tr}(\mathbf{E}_e) = \ln(J_e)\,. \tag{65}$$

Fig. 2(a) compares this expressions for moderate elastic deformations, showing very similar responses.

To compare the deviatoric strains, consider simple shear for which the velocity gradient $\mathbf{L}$ is given

$$\mathbf{L} = \dot{\gamma}\,\mathbf{e}_1\otimes\mathbf{e}_3, \tag{66}$$

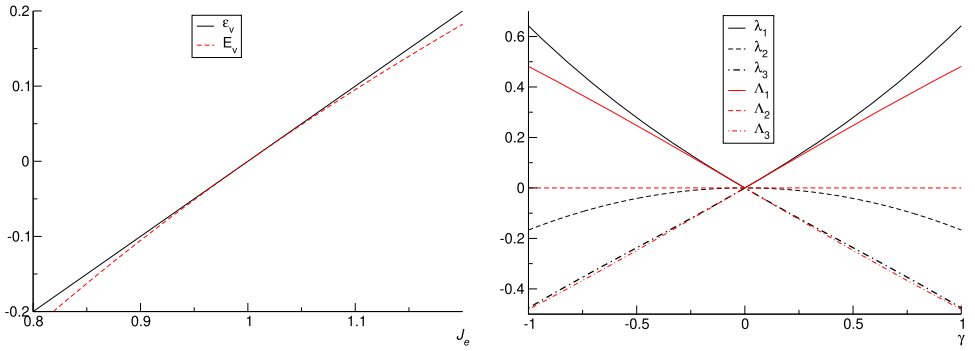

Fig. 2. (a) Comparison of the volumetric strains ε_v and E_v in (65); (b) Comparison of the eigenvalues λ_i of $\boldsymbol{\varepsilon}'_e$ and Λ_i of $\mathbf{E}'_e$ in (67) for simple shear.

where $\mathbf{e}_i$ is a fixed orthonormal triad and γ is the engineering shear strain, which vanishes in the reference configuration with $\boldsymbol{\varepsilon}'_e = \mathbf{E}'_e = \mathbf{0}$.

The eigenvalues λ_i of $\boldsymbol{\varepsilon}'_e$ for the B_e model and the eigenvalues Λ_i of $\mathbf{E}'_e$ for both the LN and LN-MD models are given by

$$\begin{aligned} &\lambda_1 = \frac{1}{12}\gamma^2 + \frac{1}{2}\sqrt{\frac{\gamma^4}{4}+\gamma^2}, \qquad \lambda_2 = -\frac{1}{6}\gamma^2, \qquad \lambda_3 = \frac{1}{12}\gamma^2 - \frac{1}{2}\sqrt{\frac{\gamma^4}{4}+\gamma^2}, \\ &\Lambda_1 = \frac{1}{2}\ln\left(1+\frac{\gamma^2}{2}+\sqrt{\frac{\gamma^4}{4}+\gamma^2}\right), \qquad \Lambda_2 = 0, \qquad \Lambda_3 = \frac{1}{2}\ln\left(1+\frac{\gamma^2}{2}-\sqrt{\frac{\gamma^4}{4}+\gamma^2}\right). \end{aligned} \tag{67}$$

Furthermore, note that the eigenvalues in Eq. (67) are ordered

$$\lambda_1 \geq \lambda_2 \geq \lambda_3, \quad \Lambda_1 \geq \Lambda_2 \geq \Lambda_3\,. \tag{68}$$

From Fig. 2(b), which plots the eigenvalues for simple shear, it is clear that for moderate elastic deformations the LN, LN-MD, and B_e models predict similar responses ($\lambda_1 \approx \Lambda_1$ and $\lambda_3 \approx \Lambda_3$), but for large elastic deformations the predictions are in general different.

In particular, notice that Eq. (66) yields isochoric deformation, such that, although λ_2 is nonzero, $\Lambda_2 = 0$, thus confirming the general results presented in Section 3.4. Hence, for plane-strain isochoric deformations, the constitutive model (37) predicts vanishing component of $\boldsymbol{\tau}$ normal to the plane. In contrast, for the B_e model the normal component of $\boldsymbol{\tau}$ does not vanish. This difference can have a significant impact on the Lode angle in the elastoplastic regime and constitutes a fundamental reason for the different responses observed in the following benchmark problems under plane-strain conditions.

7.2. Plane-strain cyclic shearing of a square block

Under plane-strain conditions, consider the square block depicted in Fig. 3a, which has edge length $H = 1$ m. The block is clamped at its bottom, has traction free lateral sides, and it is subjected to a uniform horizontal displacement and zero vertical displacement of the top edge.

The loading history consists of three steps: first, the top edge undergoes uniform horizontal displacement, increasing incrementally up to a maximum of $0.3H$ in the positive X direction. In the second step, this displacement is gradually reduced to a minimum of $-0.3H$. Finally, in the third step, the horizontal displacement is returned to zero, forcing the top edge of the block to return to its original position.

For both hypoelastic and hyperelastic simulations, a fixed time increment equal to $t_0/10$ has been set to integrate the loading history, resulting in a total of 30 load steps to complete the analysis. Here, t_0 denotes the total load time of each step, in which the applied displacement varies linearly. It should be noted that t_0 is introduced as a dummy parameter since the constitutive models are rate-independent. In the case of elastoplastic simulations, the automatic time stepping procedure available in Abaqus has been adopted. An initial time increment of $t_0/100$ has been specified. The maximum time increment has been set to $t_0/100$ for steps 1 and 2, and to $2.5t_0/100$ for step 3.

The material properties are defined by Young's modulus $E = 206$ GPa and Poisson's ratio $\nu = 0.29$, corresponding to

$$K = 163 \text{ GPa}, \quad \mu = 79.8 \text{ GPa}, \tag{69}$$

and the hardening function specified by

$$\begin{aligned} &\kappa_Y = \frac{\tau_Y}{\mu}, \quad \tau_Y = \tau_0 + (\tau_\infty - \tau_0)\left[1 - \exp\left(-\delta\varepsilon_p\right)\right] + H_Y\varepsilon_p, \\ &\tau_0 = 450 \text{ MPa}, \quad \tau_\infty = 715 \text{ MPa}, \quad \delta = 16.93, \quad H_Y = 129.24 \text{ MPa}\,, \end{aligned} \tag{70}$$

where τ_0 is the initial yield stress, which reaches the saturation value τ_∞ at a rate governed by the material parameter δ, and H_Y is a hardening modulus governing the linear part of the isotropic hardening.

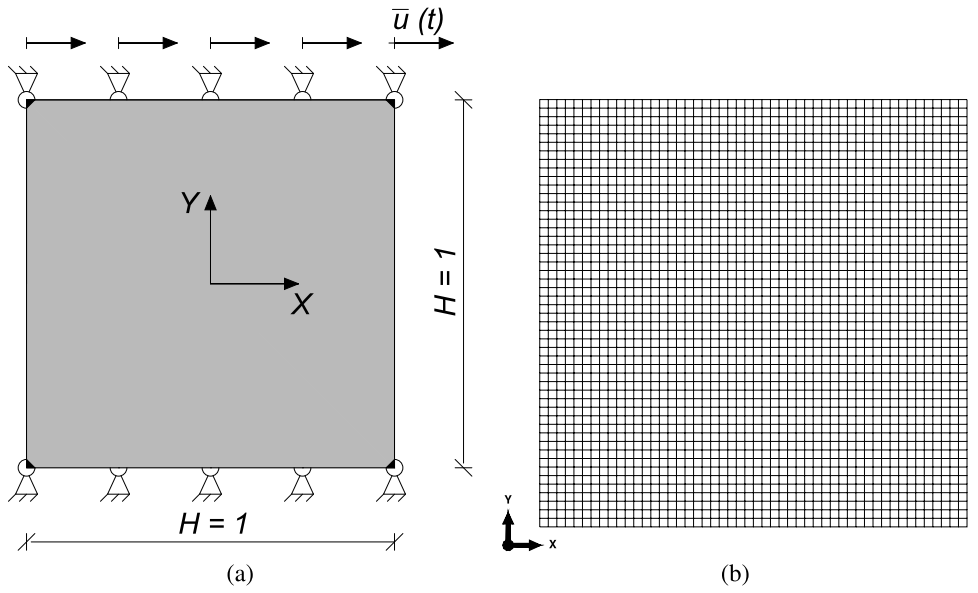

Fig. 3. Plane-strain cyclic shearing of a block: (a) geometry and boundary conditions and (b) undeformed mesh. Here, the units are in m.

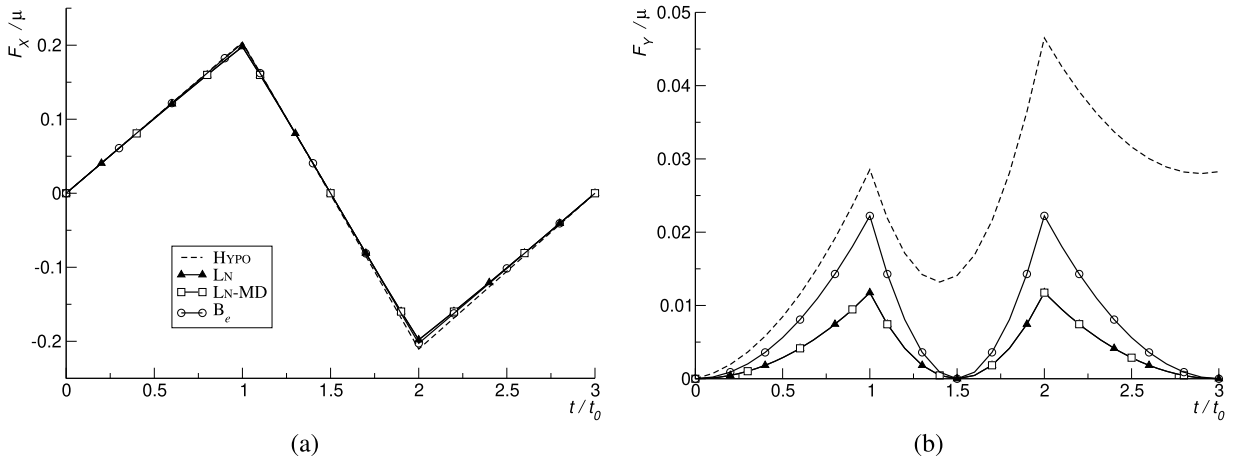

Fig. 4. Elastic response to cyclic shearing: (a) shear reaction force and (b) normal reaction force predicted by the HYPO, LN, LN-MD, and B_e models.

As displayed in Fig. 3b, the problem is discretized with a structured undeformed mesh constructed by 2500 eight-noded (i.e. bi-quadratic) FEs, each having a square shape. Reduced integration is adopted, such that each FE has four Gauss points. The analysis is performed for both elastic and elastoplastic responses, considering both von Mises and Tresca plasticity.

7.2.1. Computational efficiency

The numerical performances of the models (HYPO, LN, LN-MD, B_e) are summarized in Table 2. From this Table it can be observed that the number of loading steps for the four models is nearly the same for each of the different material responses. However, the total iterations for the simulations are different. In particular, in the absence of plasticity, the B_e and the LN-MD models significantly out-perform the HYPO and the LN models. For both the von Mises and Tresca materials the performance of the HYPO, LN-MD, and B_e models is about the same and they clearly out-perform the LN model. The comparison between the LN and LN-MD models demonstrates the importance of the modifications characterizing the LN-MD model documented in Appendices C and D.

7.2.2. Hypo/hyper-elastic responses

Predictions of the four models HYPO, LN, LN-MD, and B_e are shown in Fig. 4 for the horizontal (shear) and vertical (normal) reaction forces for elastic response as functions of time t, normalized by the time t_0 required to complete a loading ramp. Contours of the von Mises stress and deformed shapes of the block are shown in Fig. 5 at the end of the reverse loading and in Fig. 6 after the block's top surface has returned to its initial position. From these figures it can be observed that the predictions of the shear reaction force Fig. 4a are close for all four models but not for the normal force in Fig. 4b. These results for the normal force are consistent with the differences predicted for the eigenvalues shown in Fig. 2b. From Fig. 5 it is observed that the stress contours are reasonably

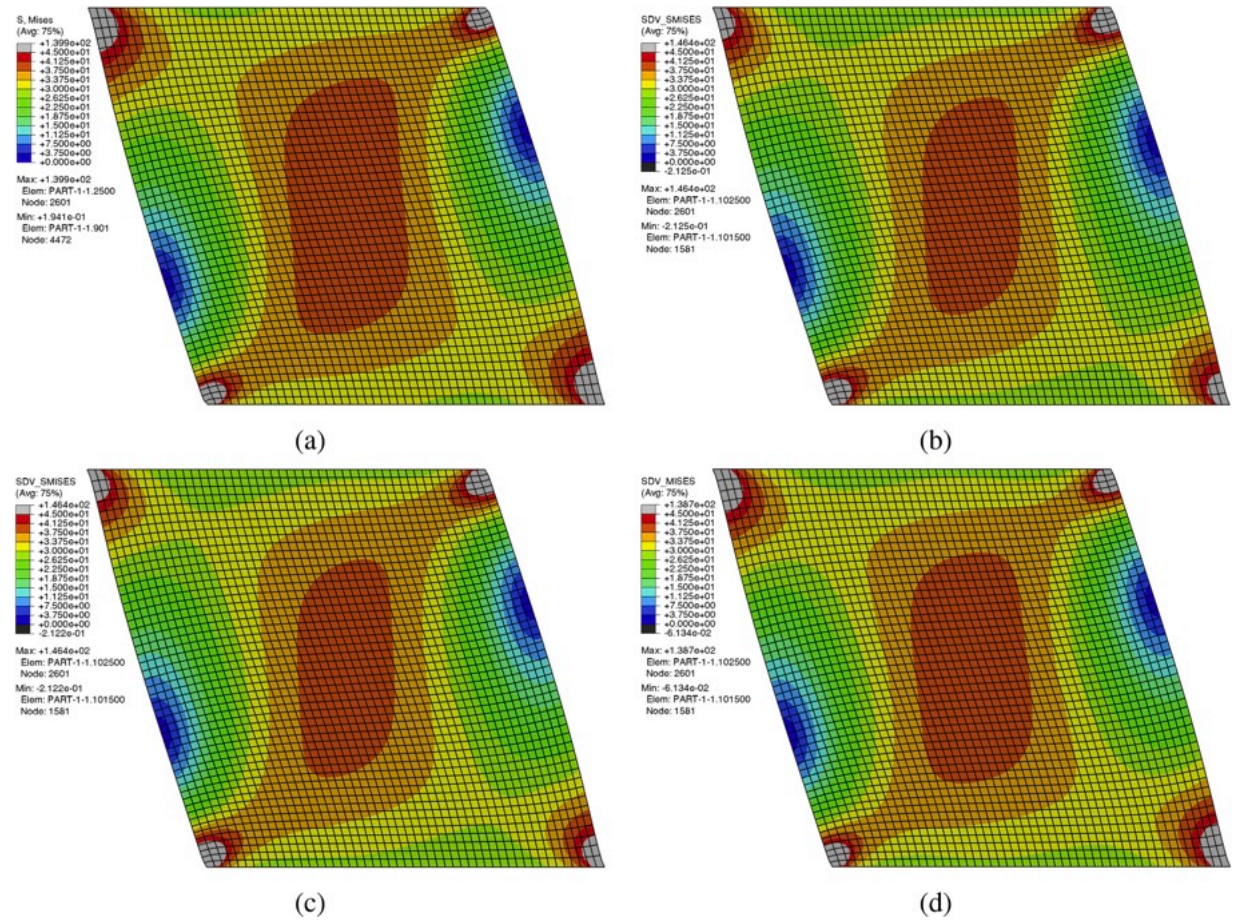

Fig. 5. Hypo/hyper-elastic responses to cyclic shearing: Contours of von Mises stress at the end of the reverse loading predicted by the models (a) HYPO, (b) LN, (c) LN-MD, and (d) B_e.

Table 2
Cyclic shearing of a block: numerical performances of the models considered.

Model	No plasticity		von Mises		Tresca	
	Loading steps	Total iterations	Loading steps	Total iterations	Loading steps	Total iterations
HYPO	30	78	267	620	275	677
LN	30	160	275	964	319	1250
LN-MD	30	56	262	603	279	682
B_e	30	43	270	648	277	683

close at the end of the reverse loading. However, as expected, the HYPO model does not predict hyperelastic response, as is seen by the nonzero value of the shear force in Fig. 4b and the finite residual stresses in Fig. 6. In contrast, the residual stresses when the block's top surfaces has returned to its initial position are small for the LN model and almost vanishing for the LN-MD and B_e models, as they should be for hyperelastic response.

Observe that the unloading condition is particularly challenging for the LN model because it involves transitioning from distinct to coincident eigenvalues for distortional deformation. Handling such repeated eigenvalues requires specific numerical treatment of the spectral theorem, and difficulties in this regard increase numerical errors. In contrast, the LN-MD model employs an approximate, yet accurate, derivative of the logarithm of the tensor differently and it is less affected by the foregoing issue, resulting in a more stable stiffness matrix and better performance under these critical conditions.

7.2.3. Elastoplastic response

Figs. 7 and 8 show contours of the von Mises stress and the deformed shapes for von Mises and Tresca plasticity, respectively. Also, Fig. 9a and b show predictions of the shear force and the normal force for the full cycle of loading, again for von Mises and Tresca

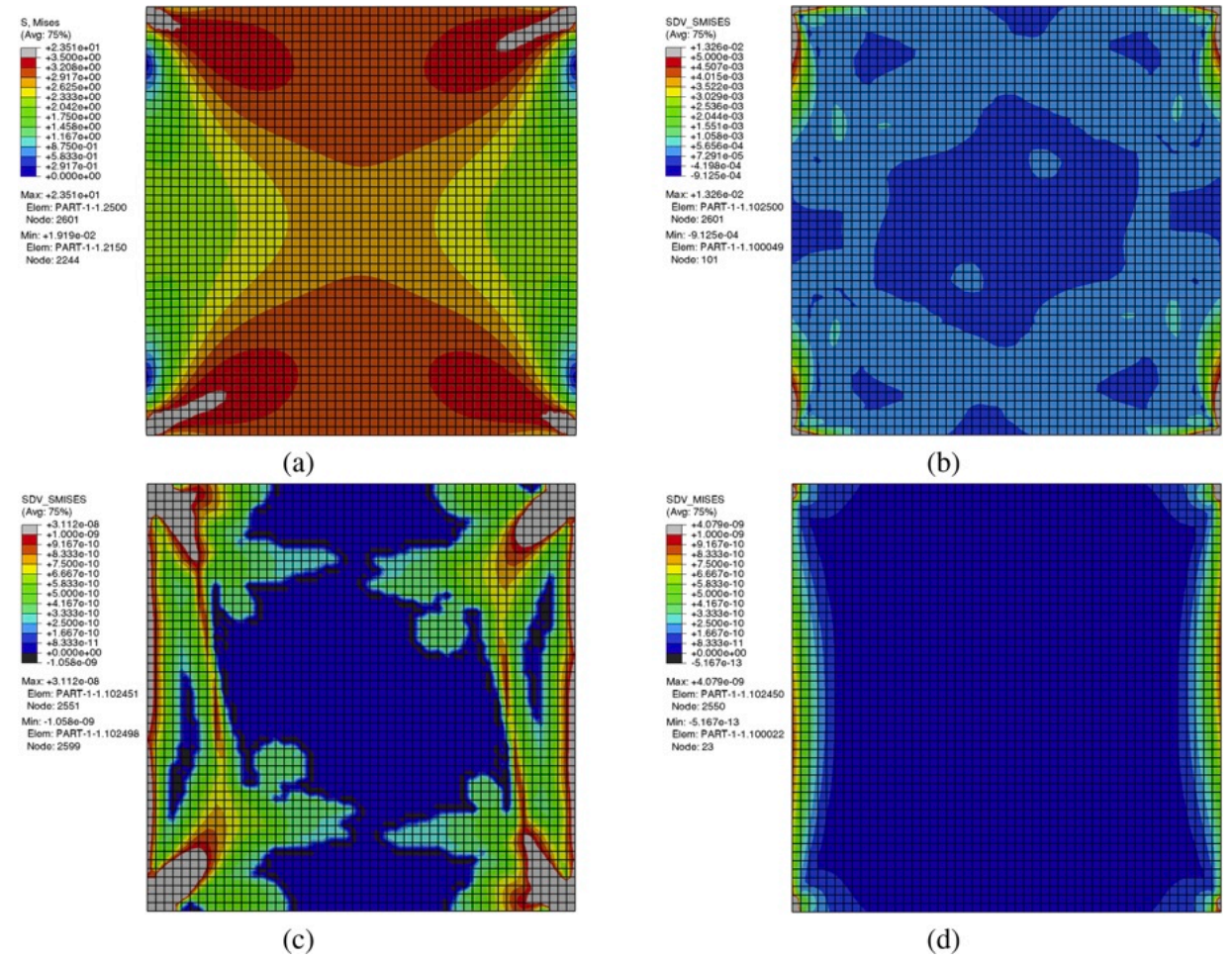

Fig. 6. Hypo/hyper-elastic responses to cyclic shearing: Residual von Mises stresses, after the loaded surface of the block is returned to its original position, predicted by the models (a) HYPO, (b) LN, (c) LN-MD, and (d) B_e.

plasticity, respectively. Since the elastic deformations during large-deformation plasticity remain relatively small, the predictions of the four models are relatively close for these simulations, with the predictions of the LN and LN-MD models being closer to those of the B_e model for both von Mises and Tresca plasticity, as can be determined by comparing the maximum stresses recorded in the figures.

Fig. 10 focuses on Tresca plasticity, for which it shows the evolution along the loading history of the stress components and of the Lode angle in the material point in the centre of the block, as predicted by the LN-MD and B_e models. The LN-MD is selected as representative of all models based on the logarithmic strain. Fig. 10a displays the in-plane stress components, which result to be almost identical for the LN-MD and B_e models. In contrast, Fig. 10b presents the evolutions of the out-of-plane stress component, of the pressure, and of the Lode angle, which are significantly different, consistently with the discussion in Section 7.1. This difference in the out-of-plane stress component, in conjunction with the model-independent in-plane stress behavior, is the reason for the pronounced discrepancies in the predictions of the equivalent von Mises stress (see, e.g., Fig. 8) and Lode angle for the logarithmic strain-based models and the B_e model.

7.3. Necking of a circular cylindrical bar

This section presents simulations of necking of a circular cylindrical bar under tension, which is a benchmark problem described in de Souza Neto et al. [11] and established since earlier contributions, such as that of Simo and Armero [72]. The bar has initial radius 6.413 mm and initial length $2H = 53.34$ mm, as illustrated in Fig. 11 along with the undeformed mesh. To trigger the necking, a geometric imperfection is introduced with the radius reduced linearly from $R_{0,\max} = 6.413$ mm at the loaded end of the bar to $R_{0,\min} = 6.35$ mm at the bar's center. The same material properties in Eqs. (69) and (70) of Section 7.2 are adopted. Due to the symmetry, only the upper half of the axisymmetric domain is discretized, using 200 8-noded, quadratic axisymmetric elements, with reduced integration (i.e. four Gauss points each). A total vertical displacement of $\bar{u} = 7$ mm is applied to the top half of the bar.

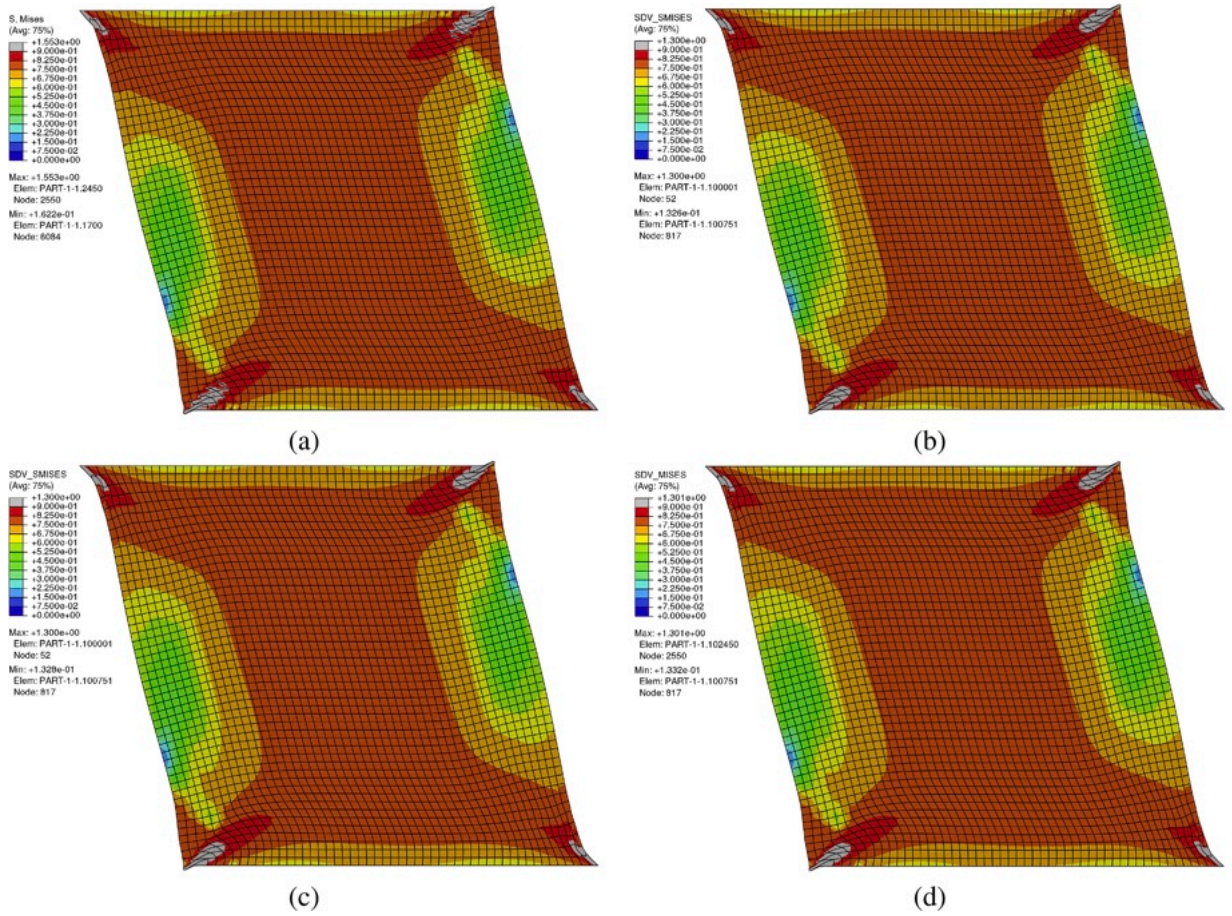

Fig. 7. Cyclic shearing using von Mises plasticity: Contours of von Mises stress at the end of the reverse loading predicted by the models (a) HYPO, (b) LN, (c) LN-MD, and (d) B_e.

Table 3
Necking of a circular cylindrical bar: Numerical performances of the models considered, for 100 fixed time increments.

Model	von Mises equilibrium iterations	Tresca equilibrium iterations
HYPO	242	315
LN	271	316
LN-MD	216	246
B_e	214	242

The necking process is simulated with the four models HYPO, LN, LN-MD, and B_e, using both von Mises plasticity and Tresca plasticity. A time-integration scheme with 100 fixed time increments has been adopted to compare the performances of the models. The numerical performances of the various models are recorded in Table 3 in terms of total number of equilibrium iterations. These results show that the numerical performance of the LN-MD and B_e models is nearly the same, although the B_e model is slightly more efficient. However, the LN-MD and B_e models are significantly more efficient than the HYPO and LN models for both von Mises and Tresca plasticity.

Fig. 12 shows the reaction force-displacement curves. Here, the force is normalized by $A_0\tau_0$, where A_0 denotes the initial value of the smallest cross-section area and τ_0 is specified in Eq. (70). For a given plasticity criterion, all models yield nearly identical results. Moreover, up to the peak stress (corresponding to $\bar{u}/H \approx 0.1$), the responses are basically independent of the adopted plasticity criterion (either von Mises or Tresca). Likely, this is due to the initially dominant uniaxial stress state.

Differences become noticeable after localization, where the models based on Tresca plasticity predict a more pronounced softening. This behavior can be ascribed to the lower shear stress levels associated with Tresca plasticity compared to the von Mises model when uniaxial stress levels are matched, leading to earlier and more intense localization phenomena.

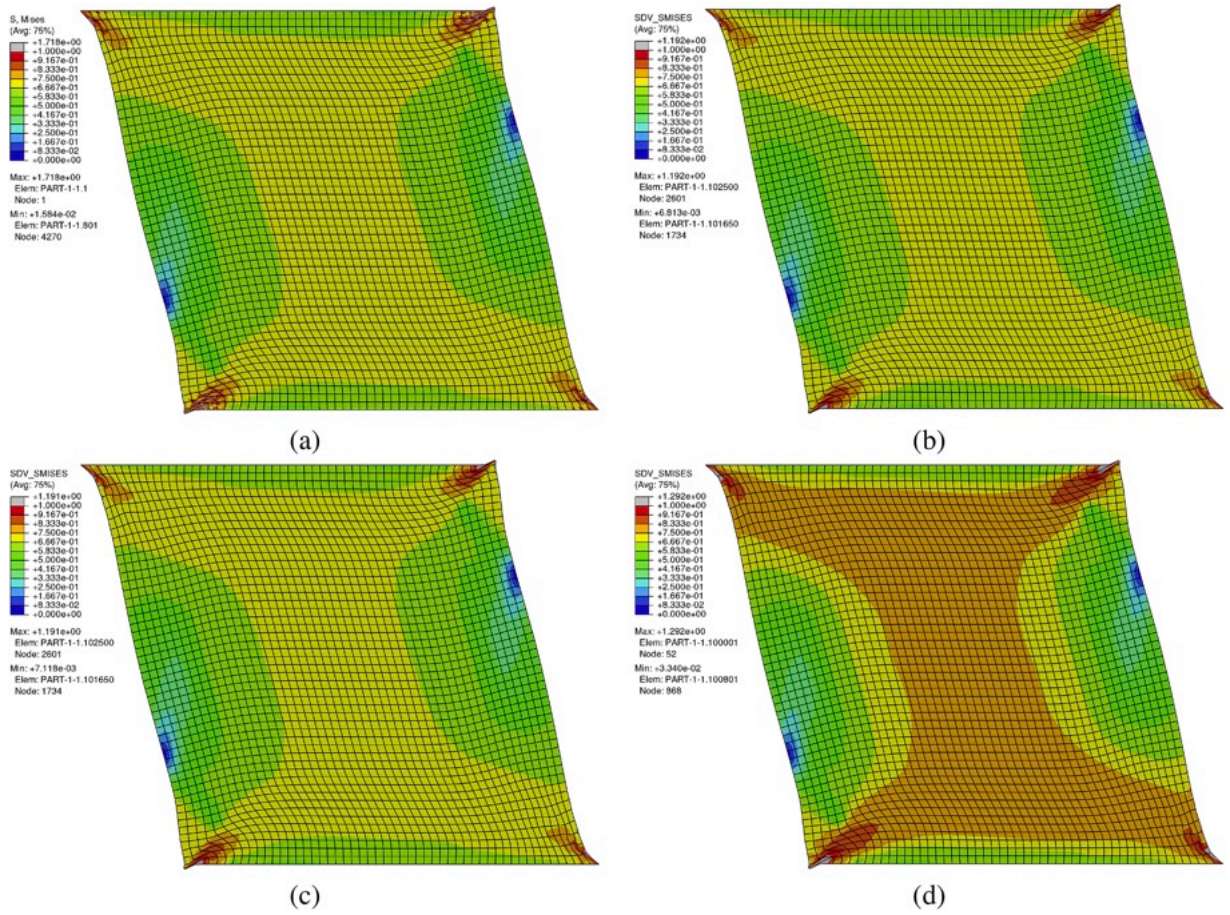

Fig. 8. Cyclic shearing using Tresca plasticity: Contours of von Mises stress at the end of the reverse loading predicted by the models (a) HYPO, (b) LN, (c) LN-MD, and (d) B_e.

Table 4
Necking of a circular cylindrical bar: Value of the normalized radial displacement at the bar's center at the end of the analysis, predicted by the models (a) HYPO, (b) LN, (c) LN-MD, and (d) B_e.

Model	Normalized radial displacement	
	von Mises	Tresca
HYPO	−0.5917	−0.6902
LN	−0.5857	−0.6646
LN-MD	−0.5857	−0.6646
B_e	−0.5861	−0.6646

Figs. 13 and 14 display the von Mises stress contours on the final deformed configuration, as predicted by the four models, for von Mises and Tresca plasticity, respectively. There predictions for this problem by all models are nearly the same.

Table 4 presents the radial displacements at the center of the bar. The displacement is normalized by dividing it by the value of the initial radius, $R_{0,\min}$, of the central cross-section of the bar, thus providing an average measure of the large reduction in radius experienced by the cross-section subject to necking. While the LN, LN-MD, and B_e models yield nearly identical results, the HYPO model predicts a radial reduction that is slightly larger for both von Mises and Tresca yield conditions. As expected, finite-deformation models based on Tresca plasticity predict a larger radial reduction in the cross-section subject to necking.

7.4. Drawing of a bar with a rectangular cross-section

This section considers the drawing benchmark problem studied in Panteghini [49]. Specifically, a bar of total length of 180 mm has a rectangular cross-section which initially measures 33.5 mm × 20 mm and is then reduced to a final geometry of 31.91 mm

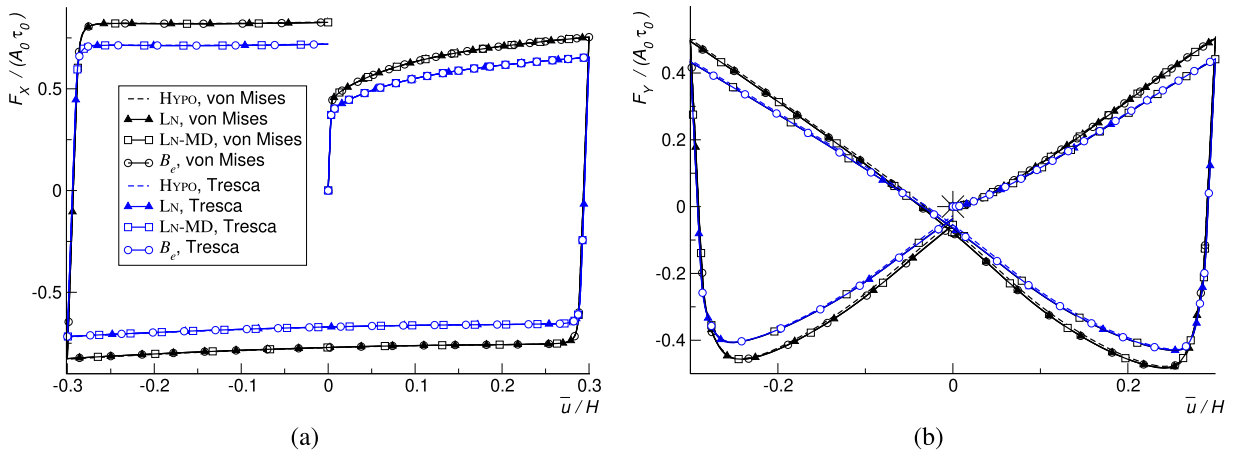

Fig. 9. Cyclic elastoplastic shearing: (a) shear reaction force and (b) normal reaction force at the loaded surface of the block predicted by the models HYPO, LN, LN-MD, and B_e for both von Mises and Tresca plasticity.

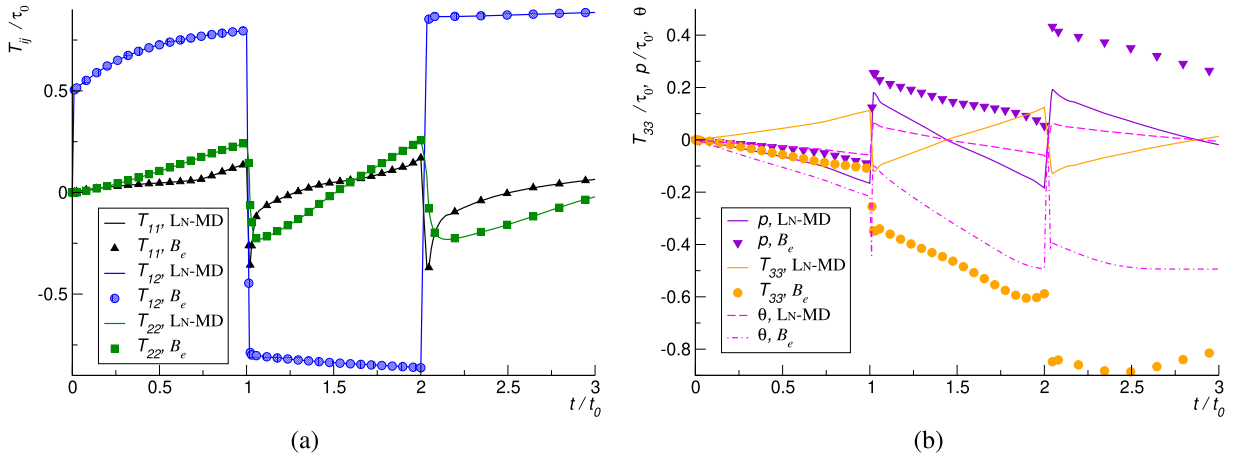

Fig. 10. Cyclic elastoplastic shearing: (a) in-plane stress components and (b) out-of-plane stress component, pressure, and Lode angle predicted by the LN-MD and B_e models for Tresca plasticity. The stress fields are non-dimensionalized by the initial yield stress τ_0 and the Lode angle is expressed in radians.

× 17.88 mm. The inlet die angle (denoted as 2α in Panteghini [49]) is set to 8°, while the other inlet die angle (denoted as 2β in Panteghini [49]) is determined by the assumption that the bar is initially in contact with all die surfaces simultaneously. The die is assumed to be rigid and the contact interaction between the bar and the die is modeled by a Coulomb node-to-surface approach, with the friction coefficient equal to 0.035.

The bar is made of $C45$ steel with the material properties defined by Young's modulus $E = 200$ GPa and Poisson's ratio $\nu = 0.30$, corresponding to

$$K = 167 \text{ GPa}, \quad \mu = 76.9 \text{ GPa}, \tag{71}$$

and the hardening function specified by

$$\kappa_Y = \frac{\tau_Y}{\mu}, \quad \tau_Y = \tau_0 + C\varepsilon_p^n, \quad \tau_0 = 345\,\text{MPa}, \quad C = 666.7\,\text{MPa}, \quad n = 0.30\,. \tag{72}$$

As illustrated in Fig. 15, a structured mesh of 56,370 3D linear brick FEs, each with eight Gauss integration points,[7] is used to discretize the bar. Due to symmetry conditions, only one quarter of the problem domain is modeled. The semi-edges of the cross-section are divided into 12 segments, while the bar length is subdivided into 180 parts. Overall, the FE model has 105,375 degrees of freedom.

[7] Note that, in general, full-integrated linear FEs may cause volumetric locking due to plastic incompressibility, particularly in the presence of large distortional plastic strains. However, the present simulations are negligibly affected by this issue. This has been verified by comparing the results presented in Fig. 16 with those obtained with the HYPO model and Abaqus' hybrid pressure-displacement elements (C3D8H). The results are in excellent agreement both for Tresca plasticity and for von Mises plasticity.

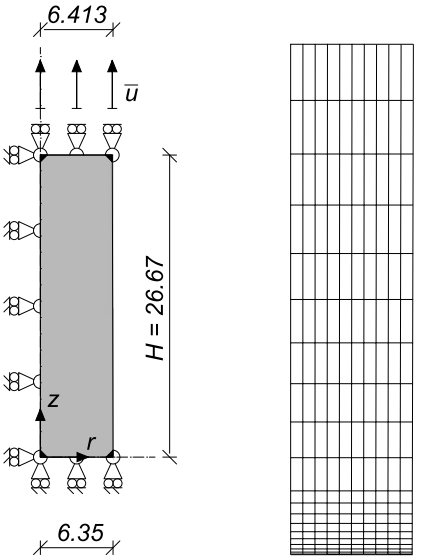

Fig. 11. Necking: Initial geometry, boundary conditions, and undeformed mesh. The left edge of the mesh belongs to the centerline z of the bar and the bottom edge of the mesh corresponds to a symmetry plane. Here, the units are in mm.

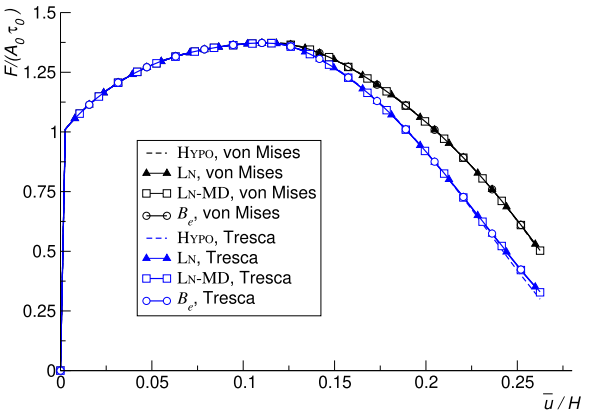

Fig. 12. Necking: Stress-strain curves showing softening for both von Mises and Tresca plasticity predicted by the HYPO, LN, LN-MD, and B_e models.

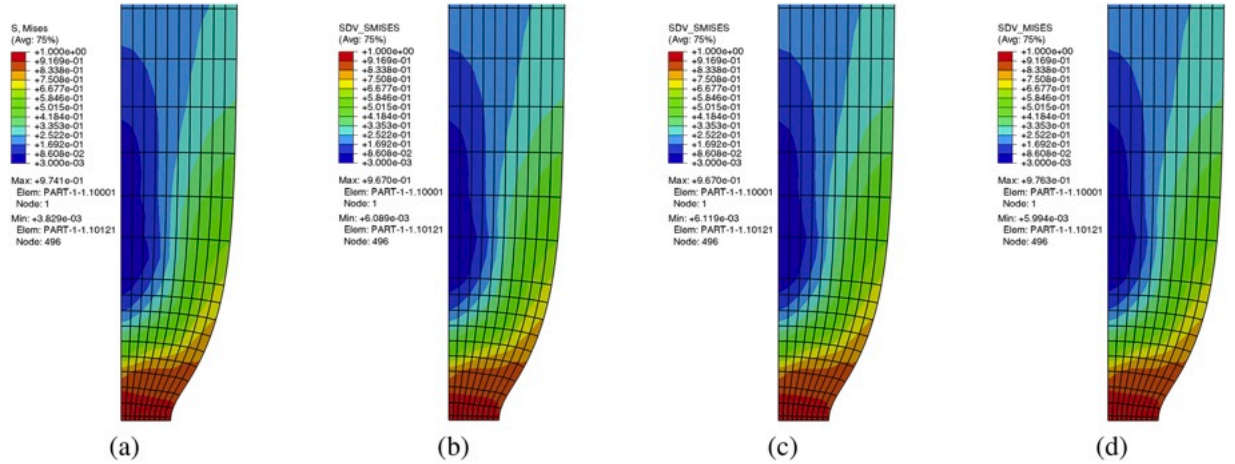

Fig. 13. Necking of a circular cylindrical bar using von Mises plasticity: Contours of the von Mises stress predicted by the models (a) HYPO, (b) LN, (c) LN-MD, and (d) B_e.

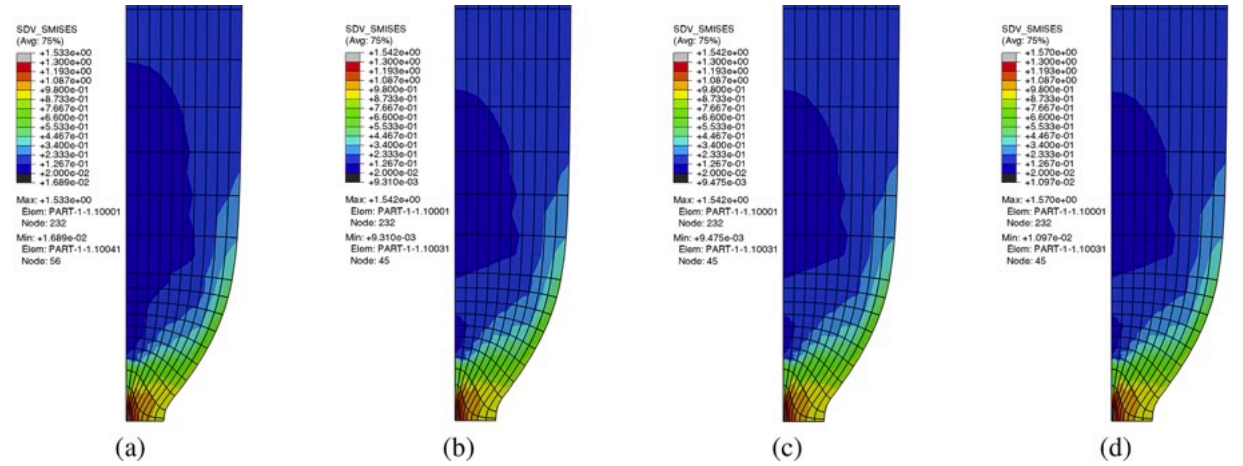

Fig. 14. Necking of a circular cylindrical bar using Tresca plasticity: Contours of the von Mises stress predicted by the models (a) HYPO, (b) LN, (c) LN-MD, and (d) B_e.

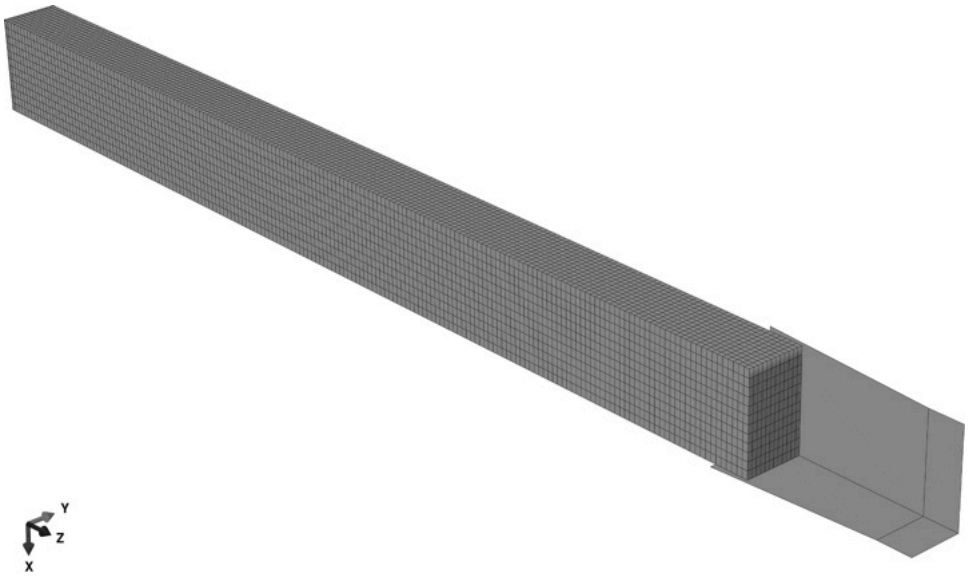

Fig. 15. Undeformed mesh and initial geometry for the bar drawing process. This mesh models one quarter of the cross-section.

The simulation has been conducted under displacement control, by prescribing a total axial displacement of 300 mm (i.e., 5/3 of the initial total length of the bar) directly to the surface nodes located at the inlet end of the bar, that is, those initially closest to the die. The applied displacement increases linearly in a total time t_0. These boundary nodes are uniformly moved along the axial direction (z in Fig. 15) in order to pull the bar through the die and reproduce the drawing process under tensile loading. The analysis has been carried out by using the automatic time stepping procedure available in Abaqus, with an initial time increment set to $t_0/150$. The maximum allowed time increment has been set equal to t_0.

Although the numerical model is based on Panteghini [49], in this study the contact interaction is modeled by resorting to a node-to-surface approach, instead of the surface-to-surface one adopted in Panteghini [49], due to the use of user-defined FEs (`uel`) in Abaqus, which do not support surface-to-surface interactions. As a further difference, Panteghini [49] employs hybrid displacement-pressure FEs.

The simulations are conducted by using only the three models HYPO, LN-MD, and B_e, but still by considering both von Mises and Tresca plasticity. In fact, as formulated, the LN model is applicable to 2D problems only, so it cannot be used for this 3D drawing problem. The numerical performances of the models, which are recorded in Table 5, indicate that all three models HYPO, LN-MD, and B_e cannot complete the simulation for von Mises plasticity. The HYPO model ceases to converge after only 16.6 % of the simulation process. For von Mises plasticity, the models LN-MD and B_e cease to converge when the last row of elements of the bar attempts to exit the die. This is also the simulation stage when the HYPO model ceases to converge for Tresca plasticity. This convergence issue is likely due to the severe distortion experienced by the back end of the bar, which is completely free and subject to significant warping.

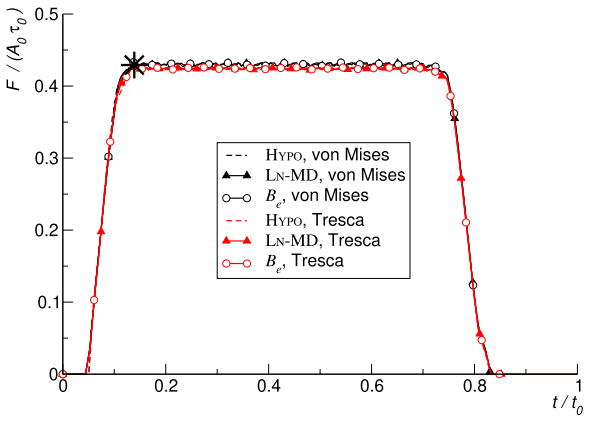

Fig. 16. Drawing force as a function of time for the Hypo and B_e models, using von Mises and Tresca plasticity. The large star indicates the point at which the Hypo model ceases to converge for von Mises plasticity.

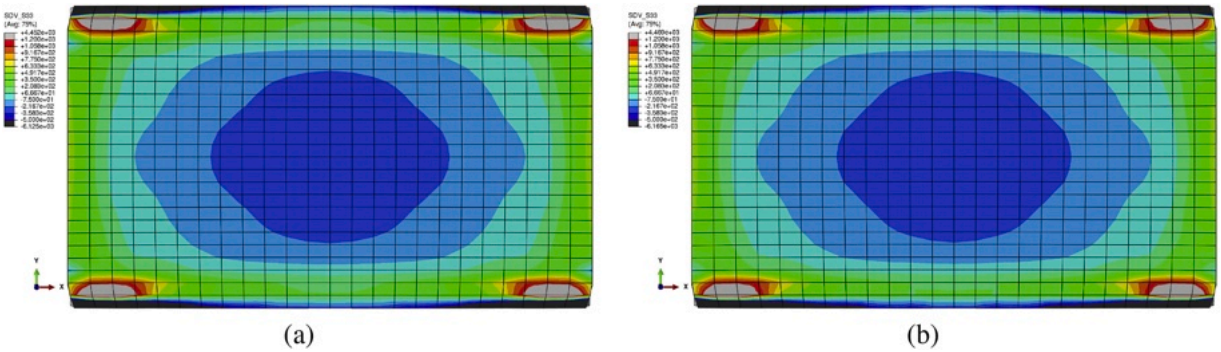

Fig. 17. Contours of the axial longitudinal stress at the end of the drawing process in the middle section of the bar for the (a) Ln-MD model and the B_e model using Tresca plasticity.

Table 5
Drawing simulation: numerical performances of the Hypo, Ln-MD, and B_e models.

Model	% Completed	Loading steps	Total Iterations	Equilibrium Iterations
von Mises				
Hypo	16.6 %	187	1276	1043
Ln-MD	99.4 %	855	4490	2098
B_e	98.6 %	783	4320	1965
Tresca				
Hypo	99.4 %	3864	20838	17151
Ln-MD	100 %	1451	7776	4551
B_e	100 %	1531	8034	4840

Instead, for Tresca plasticity, the Ln-MD and B_e models successfully complete the simulation. Moreover, from Table 5, it can be seen that the performances of the Ln-MD and B_e models are far better than that of the Hypo model.

Fig. 16 shows the normalized drawing force, $F/(A_0\tau_0)$, as a function of the non-dimensional time, with A_0 and t_0 denoting the initial cross-section area and dummyTXdummy– the total simulation time, respectively. This drawing force is lower for Tresca plasticity than for von Mises plasticity. In Fig. 16, the point where the Hypo model ceases to converge is indicated by a large star. The three models, when successful, predict similar values of the drawing force.

For Tresca plasticity, Fig. 17 presents contours of the axial longitudinal residual stress in the middle of the bar at the end of the analysis, for the models that completed the simulation, i.e. the Ln-MD and B_e models. From this figure it can be seen that the solutions predicted by these two models are nearly identical.

Finally, from an engineering perspective, the foregoing analyses allow inferring that the finite-deformation models considered provide very similar results, thus demonstrating their equivalence in predicting the large-deformation behavior under monotonic

loading conditions. Overall, the ease of implementation and the performance of the B_e model suggest advantages of that model for the benchmark problems analyzed.

8. Concluding remarks

This investigation has assessed different formulations for finite-deformation elastoplasticity dependent on the Lode angle, focusing on both accuracy and computational efficiency. The study is limited to pressure-independent yield functions and isotropic response. A general yield function, as proposed in Lagioia and Panteghini [36], has been considered, which can be specialized to classical criteria, including, among others, von Mises, Galileo, and smooth approximations of Tresca and Mohr-Coulomb.

Four finite-deformation constitutive models have been analyzed: one hypoelasto-plastic, denoted as HYPO model; two hyperelasto-plastic, both based on the logarithmic strain [19] and denoted as LN and LN-MD models; one hyperelasto-plastic, based on the left Cauchy-Green strain and denoted as B_e model. The HYPO, LN, LN-MD models share the fundamental feature of determining the elastic strain by computing the logarithm of a symmetric positive-definite second-order tensor. The HYPO model is the one included in the commercial FE software Abaqus [10]. The LN and LN-MD models differ by the way they deal with the computation of the derivative of the logarithmic elastic strain.

Specifically, the LN model is as presented in de Souza Neto et al. [11], including its implementation, the latter being provided in detail by de Souza Neto et al. [11] in a version holding for 2D problems only. Instead, the LN-MD model as implemented here is applicable to 3D problems and determines the logarithmic strain by using projection operators developed in Luehr and Rubin [41], Sylvester [76] and the exact rates of the eigenvalues discussed in Appendix D, without the need to determine ordered eigenvectors that can change orientation when two eigenvalues are coincident. Importantly, the derivatives in (D.2) are insensitive to potential multiplicity of eigenvalues, which can create significant numerical errors, since $\mathbf{B}_e$ is of order unity and $\mathbf{B}'_e$ can be small.

The B_e model adopts the Eulerian formulation of the constitutive equations proposed in Rubin [61]. Also, the B_e model is characterized by a hyperelastic response, but, instead of using the logarithmic strain, it relies on an evolution equation for the symmetric unimodular elastic distortional deformation tensor $\bar{\mathbf{B}}_e$, that coincides with the left Cauchy-Green tensor in the absence of plasticity. This equation for $\bar{\mathbf{B}}_e$ is characterized by the distortional plastic rate, which is proportional to a symmetric second-order tensor $\mathbf{A}_p$. One of the novelty of this work is the modification of $\mathbf{A}_p$ to incorporate the influence of the Lode angle.

The dependence of the plastic rate direction on the Lode angle complicates the time integration, since the derivative of the Lode angle with respect to the stress tensor is undefined when two principal stress components coincide. To address this issue, the return mapping has been formulated in terms of stress invariants, as formerly proposed, in the framework of small strains and rotations, in Panteghini and Lagioia [51,52]. This algorithm is applied to all models implemented in this investigation. Additionally, this work emphasizes that some numerical algorithms developed for small-deformation elastoplasticity can be employed for large-deformation elastoplasticity not only in the most commonly adopted approach [11,71], but also in the B_e model, which avoids the use of the logarithmic strain in favor of the computationally more convenient elastic strain in Eq. (3).

The numerical performance and the accuracy of the HYPO, LN, LN-MD, and B_e models are compared for three engineering problems, always using both von Mises plasticity and Tresca plasticity and involving remarkably large deformations. The benchmark problems analyzed are: the plane-strain cyclic shearing of a square block; the necking of a circular cylindrical bar (taken from de Souza Neto et al. [11]); and the drawing of a bar with a rectangular cross-section (taken from Panteghini [49]).

The results indicate that all four models provide very similar the accuracy, except for large elastic deformations, leading to known issues in the HYPO model (see, e.g., [75]), which, in the absence of plasticity, does not ensure stress independence upon the strain path and fails to guarantee that the work done in a closed strain path vanishes. About the computational efficiency, the LN-MD and B_e models exhibit comparable performances and outperform the LN model. However, the B_e model has the advantage over the other models of being easier to implement, as it avoids the computation of the logarithmic strain and its derivative.

It is noted that hyperelastic constitutive equations for stress are expressed in terms of derivatives of a strain-energy function and the choice of the strain measure. Specifically, different strain-energy functions and different strain measures lead to different constitutive equations for stress, all of which can be thermomechanically consistent. In this sense, the specific choice of the strain energy and strain measure is motivated by possible simplifications that may be adequate to model desired material responses. Since small elastic deformation response is unique, it only makes sense to compare different nonlinear constitutive equations that predict the same small-deformation response. The examples in this paper have shown that for isotropic elastoplastic response of metals with small elastic strains, the predictions of the models LN-MD and B_e are almost identical.

Among the open issues for future investigations, it is worth mentioning the extensions and modifications to model (i) pressure-dependent yield functions and plastic dilatation; (ii) directional/anisotropic hardening; (iii) single-crystal plasticity; (iv) small-scale size-dependent plasticity. Specifically, investigating yield functions dependent not only on the second and third invariants, but also on pressure, and considering plastic dilatation should be accompanied with a careful and thorough experimental campaign in order to discern which finite-deformation elastoplastic model better represents the response of specific materials.

CRediT authorship contribution statement

Andrea Panteghini: Writing – review & editing, Writing – original draft, Visualization, Validation, Software, Methodology, Investigation, Formal analysis, Data curation, Conceptualization; **M. B. Rubin:** Writing – review & editing, Writing – original draft, Validation, Methodology, Investigation, Formal analysis, Data curation, Conceptualization; **Lorenzo Bardella:** Writing – review & editing, Writing – original draft, Validation, Methodology, Investigation, Formal analysis.

Data availability

Data will be made available on request.

Declaration of competing interest

The authors declare that they have no known competing financial interests or personal relationships that could have appeared to influence the work reported in this paper.

Acknowledgements

The authors would like to thank K. Heiduschke for helpful comments on the Henky strain. The finite element code ABAQUS/Simulia has been run at the Department of Civil, Environmental, Architectural Engineering and Mathematics, University of Brescia, Italy, under an academic license. A.P. and L.B. acknowledge the support of the Italian Ministry of Education, University, and Research (MIUR). Work done under the auspices of GNFM (Gruppo Nazionale per la FisicaMatematica) of INDAM (Istituto Nazionale di Alta Matematica Francesco Severi).

Appendix A. Mathematical details

Using the invariants defined in Eq. (27), the definitions of $\mathbf{U}', \mathbf{N}'$ in Eqs. (39), (40) and the Cayley-Hamilton theorem for $\bar{\mathbf{B}}_e$ it follows that

$$\begin{aligned}
&-\bar{\mathbf{B}}_e^3+\beta_1\bar{\mathbf{B}}_e^2-\frac{1}{2}(\beta_1^2-\beta_2)\bar{\mathbf{B}}_e+\mathbf{I}=\mathbf{0},\\
&\bar{\mathbf{B}}_e^{-1}=\bar{\mathbf{B}}_e^2-\beta_1\bar{\mathbf{B}}_e+\frac{1}{2}(\beta_1^2-\beta_2)\mathbf{I},\\
&\beta_2=\Big(\frac{\beta_1}{3}\mathbf{I}+\bar{\mathbf{B}}'_e\Big)\cdot\Big(\frac{\beta_1}{3}\mathbf{I}+\bar{\mathbf{B}}'_e\Big)=\frac{\beta_1^2}{3}+|\bar{\mathbf{B}}'_e|^2,\\
&\mathrm{tr}(\bar{\mathbf{B}}_e)\mathrm{tr}(\bar{\mathbf{B}}_e^{-1})-9=\frac{\beta_1}{2}\Big(\beta_1^2-\beta_2\Big)-9=\frac{\beta_1^3}{3}-\frac{\beta_1}{2}|\bar{\mathbf{B}}'_e|^2-9,\\
&\mathbf{N}'\cdot\bar{\mathbf{B}}_e^{-1}=|\bar{\mathbf{B}}'_e|^2(\mathbf{U}'^2\cdot\mathbf{N}'),
\end{aligned}\tag{A.1}$$

Also, since $\bar{\mathbf{B}}_e$ is unimodular it follows that

$$\begin{aligned}
&\det\Big(\bar{\mathbf{B}}'_e+\frac{\beta_1}{3}\mathbf{I}\Big)=-\Big(-\frac{\beta_1}{3}\Big)^3+\frac{1}{2}|\bar{\mathbf{B}}'_e|^2\Big(-\frac{\beta_1}{3}\Big)+\det(\bar{\mathbf{B}}'_e)=1,\\
&\Big(\frac{\beta_1}{3}\Big)^3-\frac{1}{2}|\bar{\mathbf{B}}'_e|^2\frac{\beta_1}{3}+\frac{1}{3}\mathrm{tr}(\bar{\mathbf{B}}'^3_e)-1=0,\\
&\frac{\beta_1^3}{3}-\frac{3\beta_1}{2}|\bar{\mathbf{B}}'_e|^2+3|\bar{\mathbf{B}}'_e|^3\mathrm{tr}(\mathbf{U}'^3)-9=0,\\
&\frac{\beta_1^3}{3}-\frac{\beta_1}{2}|\bar{\mathbf{B}}'_e|^2-9=\beta_1|\bar{\mathbf{B}}'_e|^2-3|\bar{\mathbf{B}}'_e|^3\mathrm{tr}(\mathbf{U}'^3),
\end{aligned}\tag{A.2}$$

where use has been made of the expression

$$\mathrm{tr}(\bar{\mathbf{B}}'^3_e)=3\det(\bar{\mathbf{B}}'_e).\tag{A.3}$$

Furthermore, it can be shown that

$$\begin{aligned}
&\mathbf{N}'\cdot\mathbf{U}'^2=\frac{2\sqrt{6}}{9}\Big[-\sin\Big(\frac{\pi}{6}+\theta\Big)\cos^2\Big(\frac{\pi}{6}+\theta\Big)+\sin^2(\theta)\cos(\theta)-\sin^2\Big(\frac{\pi}{3}+\theta\Big)\cos\Big(\frac{\pi}{3}+\theta\Big)\Big]=-\frac{\cos(3\theta)}{\sqrt{6}}\le 0,\\
&\mathrm{tr}(\mathbf{U}'^3)=\frac{2\sqrt{6}}{9}\Big[\cos^3\Big(\frac{\pi}{6}+\theta\Big)+\sin^3(\theta)-\sin^3\Big(\frac{\pi}{3}+\theta\Big)\Big]=-\frac{\sin(3\theta)}{\sqrt{6}}.
\end{aligned}$$

Given the value of $\bar{\mathbf{B}}'_e$ the invariant β_1 in Eq. (27) can be determined by requiring $\bar{\mathbf{B}}_e$ to be a unimoduluar tensor

$$\det\Big(\bar{\mathbf{B}}'_e+\frac{\beta_1}{3}\mathbf{I}\Big)=1,\quad\Big(\frac{\beta_1}{3}\Big)^3-\frac{1}{2}|\bar{\mathbf{B}}'_e|^2\frac{\beta_1}{3}+\det(\bar{\mathbf{B}}'_e)=1.\tag{A.4}$$

which yields a cubic equation for β_1 [63]

$$\beta_1^3-\frac{9}{2}|\bar{\mathbf{B}}'_e|^2\beta_1+27(\det\bar{\mathbf{B}}'_e-1)=0,\tag{A.5}$$

with the solution

$$\beta_1 = \begin{cases} 3 \quad \text{if} \quad |\bar{\mathbf{B}}'_e| = 0 \\ \sqrt{6}|\bar{\mathbf{B}}'_e| \cos\left[\frac{1}{3}\arccos\left(\sin(3\theta) + \frac{3\sqrt{6}}{|\bar{\mathbf{B}}'_e|^3}\right)\right] \\ \qquad \text{if} \quad \left|\sin(3\theta) + \frac{3\sqrt{6}}{|\bar{\mathbf{B}}'_e|^3}\right| \le 1 \\ \sqrt{6}|\bar{\mathbf{B}}'_e| \cosh\left[\frac{1}{3}\operatorname{arccosh}\left(\sin(3\theta) + \frac{3\sqrt{6}}{|\bar{\mathbf{B}}'_e|^3}\right)\right] \\ \qquad \text{if} \quad \left|\sin(3\theta) + \frac{3\sqrt{6}}{|\bar{\mathbf{B}}'_e|^3}\right| > 1 \end{cases} \tag{A.6}$$

where use has been made of Eq. (A.3). Following Lagioia et al. [37] the correct solution corresponds to the largest solution for β_1 of the cubic Eq. (A.5).

Appendix B. A strongly objective algorithm for elastic distortional deformation and hardening in the $\mathbf{B}_e$ model

The numerical integration algorithm solves the evolution Eq. (42) for $\bar{\mathbf{B}}'_e$ and Eq. (46) for ε_p, given the values

$$\left\{ \bar{\mathbf{B}}'_e(t_n), \varepsilon_p(t_n) \right\}, \tag{B.1}$$

where $\bar{\mathbf{B}}_e$ is determined by using Eqs. (A.4) and (A.6) for a given value of $\bar{\mathbf{B}}'_e$.

To integrate the evolution Eq. (26) for elastic distortional deformation it is convenient to introduce the trial value $\bar{\mathbf{B}}^*_e$, which satisfies the equations

$$\bar{\mathbf{B}}^*_e = \bar{\mathbf{F}}_r \bar{\mathbf{B}}_e(t_n) \bar{\mathbf{F}}_r^T, \quad \dot{\bar{\mathbf{B}}}^*_e = \mathbf{L}' \bar{\mathbf{B}}^*_e + \bar{\mathbf{B}}^*_e \mathbf{L}'^T, \quad \bar{\mathbf{B}}^*_e(t_n) = \bar{\mathbf{B}}_e(t_n). \tag{B.2}$$

It also follows that the deviatoric part $\bar{\mathbf{B}}^{*\prime}_e$ of the elastic trial satisfies the equations

$$\dot{\bar{\mathbf{B}}}^{*\prime}_e = \mathbf{L}' \bar{\mathbf{B}}^*_e + \bar{\mathbf{B}}^*_e \mathbf{L}'^T - \frac{2}{3}(\bar{\mathbf{B}}^*_e \cdot \mathbf{D}')\mathbf{I}, \quad \bar{\mathbf{B}}^{*\prime}_e(t_n) = \bar{\mathbf{B}}'_e(t_n). \tag{B.3}$$

Then, the evolution Eq. (42) is approximated by

$$\dot{\bar{\mathbf{B}}}'_e = \dot{\bar{\mathbf{B}}}^{*\prime}_e - \Gamma\left[\bar{\mathbf{B}}'_e + \eta|\bar{\mathbf{B}}'_e|\,\mathbf{N}'\right], \tag{B.4}$$

which is integrated using a backward Euler approximation of the derivative to obtain

$$\bar{\mathbf{B}}'_e = \bar{\mathbf{B}}^{*\prime}_e - \Delta\Gamma\left(\bar{\mathbf{B}}'_e + \eta|\bar{\mathbf{B}}'_e|\,\mathbf{N}'\right), \quad \Delta\Gamma = \Delta t\,\Gamma, \tag{B.5}$$

which predicts the exact value of $\bar{\mathbf{B}}'_e$ for elastic response with $\Delta\Gamma = 0$. Also, the solution of the evolution Eq. (46) is formulated in the implicit form

$$\varepsilon_p = \varepsilon_p(t_n) + \Delta\Gamma\varepsilon_{eq}\sqrt{1+\eta^2}. \tag{B.6}$$

The yield function f in Eq. (14) depends on the final values of ε_{eq}, θ. With the help of Eqs. (3), (10), and (11), the value of ε_{eq} at the end of the time step is given by

$$\varepsilon_{eq} = |\bar{\mathbf{B}}'_e|/\sqrt{6}. \tag{B.7}$$

Taking the inner product of Eq. (B.5) with $\mathbf{N}'$ yields

$$\Delta\Gamma\eta|\bar{\mathbf{B}}'_e| = \bar{\mathbf{B}}^{*\prime}_e \cdot \mathbf{N}', \tag{B.8}$$

which can be substituted into Eq. (B.5) to obtain

$$\bar{\mathbf{B}}'_e = \frac{\bar{\mathbf{B}}^{*\prime}_e - (\bar{\mathbf{B}}^{*\prime}_e \cdot \mathbf{N}')\mathbf{N}'}{1+\Delta\Gamma}, \quad |\bar{\mathbf{B}}'_e| = \frac{\sqrt{|\bar{\mathbf{B}}^{*\prime}_e|^2 - (\bar{\mathbf{B}}^{*\prime}_e \cdot \mathbf{N}')^2}}{1+\Delta\Gamma}. \tag{B.9}$$

In these expressions $\bar{\mathbf{B}}'_e$ and $\bar{\mathbf{B}}^{*\prime}_e$ have the same eigenvectors and $\bar{\mathbf{B}}^{*\prime}_e$ has the Lode angle θ^*, so that

$$\bar{\mathbf{B}}^{*\prime}_e \cdot \mathbf{N}' = |\bar{\mathbf{B}}^{*\prime}_e| \sin(\theta^* - \theta), \tag{B.10}$$

Thus, using Eqs. (B.8)–(B.10), it follows that

$$\Delta\Gamma = \frac{|\bar{\mathbf{B}}^{*\prime}_e| \sin(\theta^* - \theta)}{\eta|\bar{\mathbf{B}}'_e|}, \quad |\bar{\mathbf{B}}'_e| = \frac{|\bar{\mathbf{B}}^{*\prime}_e| \cos(\theta^* - \theta)}{1+\Delta\Gamma},$$

which can be used together with Eq. (B.9) to obtain

$$\begin{aligned}
&\Delta\Gamma = \frac{\sin(\theta^* - \theta)}{\eta\cos(\theta^* - \theta) - \sin(\theta^* - \theta)} \geq 0,\\
&|\bar{\mathbf{B}}'_e| = |\bar{\mathbf{B}}^{*\prime}_e|\left[\cos(\theta^* - \theta) - \frac{1}{\eta}\sin(\theta^* - \theta)\right],\\
&\bar{\mathbf{B}}'_e = \frac{\bar{\mathbf{B}}^{*\prime}_e - |\bar{\mathbf{B}}^{*\prime}_e|\sin(\theta^* - \theta)\mathbf{N}'}{1 + \Delta\Gamma}.
\end{aligned} \tag{B.11}$$

In summary, the equivalent elastic strain ε_{eq} is defined by Eq. (11), the equivalent plastic strain ε_p is determined by Eq. (B.6), the yield function f is defined by Eq. (14), the parameter η is defined by Eq. (41), $\kappa_Y(\varepsilon_p)$ is a function that specifies hardening, $(\Delta\Gamma, \bar{\mathbf{B}}'_e)$ are determined by Eq. (B.11), and $\bar{\mathbf{B}}_e$ is determined by Eq. (A.6), which are all functions of the unknown Lode angle θ at the end of the time step.

Following the procedure described in Panteghini and Lagioia [52] the solution algorithm is as follows:

Elastic response The algorithm starts by determining the elastic trial value f^* of the yield function using the elastic values

$$\Delta\Gamma = 0, \quad \theta = \theta^*. \tag{B.12}$$

If $f^* \leq 0$, then the elastic trial values based on Eq. (B.12) determine the final values at the end of the time step.

Plastic response with constant Lode angle

If $f^* > 0$ then the response is elastoplastic. Next, the trial Lode angle θ^* is determined based on $\bar{\mathbf{B}}^{*\prime}_e$ and the trial value $\eta^* = \eta(\theta^*)$ is determined. If $\eta^* = 0$ then the final solution is obtained by specifying $\theta = \theta^*$ and iterating on the value of $\Delta\Gamma > 0$ using Eq. (B.6) and

$$\bar{\mathbf{B}}'_e = \frac{\bar{\mathbf{B}}^{*\prime}_e}{1 + \Delta\Gamma}, \tag{B.13}$$

until the value of the yield criterion f Eq. (14) vanishes.

Plastic response with variable Lode angle

If $f^* > 0$ and $\eta^* \neq 0$ then the response is elastoplastic with variable Lode angle and the value of θ is iterated upon using Eqs. (B.6) and (B.13) until the yield function f in Eq. (14) vanishes with the final values of all parameters determined by this final value of θ.

Next, the consistency of the foregoing equations with those in Panteghini and Lagioia [52] is demonstrated.

Using the definition of (10) of $\boldsymbol{\varepsilon}'_e$ and defining $\boldsymbol{\varepsilon}^{*\prime}_e$ as

$$\boldsymbol{\varepsilon}^{*\prime}_e = \frac{1}{2}\bar{\mathbf{B}}^{*\prime}_e,$$

the relations in Eq. (B.11) can be rewritten in the forms

$$\begin{aligned}
&\Delta\Gamma = \frac{\varepsilon^*_{eq}\sin(\theta^* - \theta)}{\eta\varepsilon_{eq}} = \frac{\sin(\theta^* - \theta)}{\eta\cos(\theta^* - \theta) - \sin(\theta^* - \theta)},\\
&\varepsilon_{eq} = \varepsilon^*_{eq}\left[\cos(\theta^* - \theta) - \frac{1}{\eta}\sin(\theta^* - \theta)\right],\\
&\boldsymbol{\varepsilon}'_e = \frac{\boldsymbol{\varepsilon}^{*\prime}_e - \sqrt{3/2}\varepsilon^*_{eq}\sin(\theta^* - \theta)\mathbf{N}'}{1 + \Delta\Gamma}
\end{aligned} \tag{B.14}$$

It should be noted that the first of these equations can be recovered by substituting the second relation in Eq. (55) into the second relation in Eq. (54) and making use of Eq. (58). Also, the second relation in Eq. (B.14) is coincident to Eq. (59). Consequently, the relations in Eq. (B.11) are consistent with those in Panteghini and Lagioia [52].

Appendix C. Determination of the logarithm of a symmetric positive-definite second-order tensor

Let $\mathbf{B}$ be a symmetric positive-definite second-order tensor with ordered eigenvalues $(\lambda_1^2 \geq \lambda_2^2 \geq \lambda_3^2)$. Following the work in Luehr and Rubin [41], Sylvester [76], the logarithm of $\mathbf{B}$ can be expressed in the following forms, dependent on the eigenvalue multiplicity.

For three distinct eigenvalues $(\lambda_1^2 > \lambda_2^2 > \lambda_3^2)$*:*

$$\begin{aligned}
&\ln(\mathbf{B}) = \ln\left(\lambda_1^2\right)\mathbf{P}_1 + \ln\left(\lambda_2^2\right)\mathbf{P}_2 + \ln\left(\lambda_3^2\right)\mathbf{P}_3,\\
&\mathbf{P}_1 = \frac{\left(\mathbf{B} - \lambda_2^2\mathbf{I}\right)\left(\mathbf{B} - \lambda_3^2\mathbf{I}\right)}{\left(\lambda_1^2 - \lambda_2^2\right)\left(\lambda_1^2 - \lambda_3^2\right)}, \quad \mathbf{P}_2 = \frac{\left(\mathbf{B} - \lambda_1^2\mathbf{I}\right)\left(\mathbf{B} - \lambda_3^2\mathbf{I}\right)}{\left(\lambda_2^2 - \lambda_1^2\right)\left(\lambda_2^2 - \lambda_3^2\right)}, \quad \mathbf{P}_3 = \frac{\left(\mathbf{B} - \lambda_1^2\mathbf{I}\right)\left(\mathbf{B} - \lambda_2^2\mathbf{I}\right)}{\left(\lambda_3^2 - \lambda_1^2\right)\left(\lambda_3^2 - \lambda_3^2\right)}.
\end{aligned}$$

For two equal eigenvalues $(\lambda_r^2 = \lambda_1^2 = \lambda_2^2 > \lambda_{nr}^2 = \lambda_3^2)$ *or* $(\lambda_{nr}^2 = \lambda_1^2 > \lambda_r^2 = \lambda_2^2 = \lambda_3^2)$*:*

$$\ln(\mathbf{B}) = \ln\left(\lambda_r^2\right)\mathbf{P}_r + \ln\left(\lambda_{nr}^2\right)\mathbf{P}_{nr}, \quad \mathbf{P}_r = \frac{\mathbf{B} - \lambda_{nr}^2\mathbf{I}}{\lambda_r^2 - \lambda_{nr}^2}, \quad \mathbf{P}_{nr} = \frac{\mathbf{B} - \lambda_r^2\mathbf{I}}{\lambda_{nr}^2 - \lambda_r^2}.$$

For three equal eigenvalues $\left(\lambda_r^2 = \lambda_1^2 = \lambda_2^2 = \lambda_3^2\right)$*:*

$$\ln(\mathbf{B}) = \ln\left(\lambda_r^2\right)\mathbf{I}\,.$$

In these equations the projection operators $\mathbf{P}_i$ are symmetric second-order tensors having the properties

$$\mathbf{P}_i\mathbf{P}_j = 0 \quad \text{for } i \neq j, \quad \mathbf{P}_i\mathbf{P}_i = \mathbf{P}_i \text{ no sum on } i\,.$$

It is also noted that eigenprojection tensors are used in Heiduschke [18] to study generalized strain-space formulations and in Jog [27] to study the logarithm of a second-order tensor.

Appendix D. An approximate, yet accurate derivative of the logarithm of a symmetric positive-definite tensor

Letting $\mathbf{B}$ in Appendix C be the left Cauchy-Green deformation tensor, the logarithmic strain $\mathbf{E}$ can be defined by

$$\mathbf{E} = \frac{1}{2}\ln(\mathbf{B}) = \frac{1}{4}\ln(\mathbf{B}^2)\,.$$

The material derivative of $\mathbf{E}$ is approximated by

$$\dot{\mathbf{E}} \approx \dot{\tilde{\mathbf{E}}} = \frac{1}{4}\mathbf{B}^{-1}\dot{\overline{\mathbf{B}^2}}\mathbf{B}^{-1} = \frac{1}{4}\left(\mathbf{B}^{-1}\dot{\mathbf{B}} + \dot{\mathbf{B}}\mathbf{B}^{-1}\right)\,. \tag{D.1}$$

Expressing these tensors with respect to the fixed triad $\mathbf{e}_i$ yields

$$\dot{E}_{ij} = E_{ijrs}\dot{B}_{rs},$$
$$E_{ijrs} = \frac{1}{4}\left[(\mathbf{B}^{-1})_{ir}\delta_{js} + (\mathbf{B}^{-1})_{is}\delta_{jr} + \delta_{ir}(\mathbf{B}^{-1})_{js} + \delta_{is}(\mathbf{B}^{-1})_{jr}\right],$$

where δ_{ij} denotes the Kronecker symbol and E_{ijrs} has 21 independent components since it satisfies the symmetries

$$E_{ijrs} = E_{jirs} = E_{ijsr} = E_{rsij}\,.$$

To examine the approximation in the derivative (D.1), let $\mathbf{\Lambda}$ be the skew-symmetric tensor determining the rate of rotation of the triad $\mathbf{P}_i$, such that

$$\mathbf{\Lambda}^T = -\mathbf{\Lambda}, \quad \dot{\mathbf{P}}_i = \mathbf{\Lambda}\mathbf{P}_i - \mathbf{P}_i\mathbf{\Lambda}\,. \tag{D.2}$$

Then, $\mathbf{B}$ and the Henky strain $\mathbf{E}$ can be expressed in their spectral forms, which satisfy the equations

$$\begin{aligned}
&\mathbf{B} = \sum_i^3 \lambda_i^2\mathbf{P}_i, \quad \dot{\mathbf{B}} = \sum_i^3 2\lambda_i\dot{\lambda}_i\mathbf{P}_i + \mathbf{\Lambda}\mathbf{B} - \mathbf{B}\mathbf{\Lambda}, \quad \mathbf{B}^{-1} = \sum_i^3 \frac{1}{\lambda_i^2}\mathbf{P}_i,\\
&\mathbf{E} = \sum_i^3 \ln(\lambda_i)\mathbf{P}_i, \quad \dot{\mathbf{E}} = \sum_i^3 \frac{\dot{\lambda}_i}{\lambda_i}\mathbf{P}_i + \mathbf{\Lambda}\boldsymbol{\varepsilon} - \boldsymbol{\varepsilon}\mathbf{\Lambda}\,.
\end{aligned} \tag{D.3}$$

Next, the approximation $\dot{\tilde{\mathbf{E}}}$ in (D.1) can be written as

$$\dot{\tilde{\mathbf{E}}} = \sum_i^3 \frac{\dot{\lambda}_i}{\lambda_i}\mathbf{P}_i + \frac{1}{4}(\mathbf{B}^{-1}\mathbf{\Lambda}\mathbf{B} - \mathbf{B}\mathbf{\Lambda}\mathbf{B}^{-1})\,. \tag{D.4}$$

In particular, notice that the approximation $\dot{\tilde{\mathbf{E}}}$ predicts the exact rates of eigenvalues determined by $\dot{\mathbf{E}}$

$$\dot{\tilde{\mathbf{E}}}\cdot\mathbf{P}_i = \dot{\mathbf{E}}\cdot\mathbf{P}_i = \frac{\dot{\lambda}_i}{\lambda_i}\,. \tag{D.5}$$

Thus, the only difference between $\dot{\mathbf{E}}$ and $\dot{\tilde{\mathbf{E}}}$ is the influence of the spin terms due rotation of the projection operators. This error does not influence the determination of $\mathbf{F}^{int}$ in (63), which depends on the predicted values of $\mathbf{E} = \boldsymbol{\varepsilon}$. However, the orientation of the strain tensor is determined by the equations of motion and boundary conditions, and in the LN-MD model the strain is determined using the projection operators in Appendix C. Consequently, the use of the expressions (D.2) together will the projection operators in Appendix C yield an excellent rate of convergence, as can be seen even for the nonlinear elastic response in Fig. 4. Importantly, the derivatives in (D.2) are insensitive to potential multiplicity of eigenvalues, which can create significant numerical error, since $\mathbf{B}_e$ is of order unity and $\mathbf{B}'_e$ can be small.

Appendix E. Finite element operators

E.1. Plane strain

The matrix $\mathbf{H}_p$ that contains the derivatives of the shape functions with respect to the intrinsic coordinate system $\mathbf{r}$, can be expressed as

$$\mathbf{H}_p = \begin{bmatrix} \dfrac{\mathrm{d}N^{(1)}}{\mathrm{d}r} & \cdots & \dfrac{\mathrm{d}N^{(n)}}{\mathrm{d}r} \\ \dfrac{\mathrm{d}N^{(1)}}{\mathrm{d}s} & \cdots & \dfrac{\mathrm{d}N^{(n)}}{\mathrm{d}s} \end{bmatrix}.$$

The jacobian, in the reference coordinate system, can be computed as

$$\mathbf{J}_R = \mathbf{H}_p \hat{\mathbf{X}}_R,$$

where

$$\hat{\mathbf{X}}_R = \begin{bmatrix} \hat{x}_{R,1}^{(1)} & \hat{x}_{R,2}^{(1)} \\ .. & .. \\ \hat{x}_{R,1}^{(n)} & \hat{x}_{R,2}^{(n)} \end{bmatrix}.$$

The nodal displacements are ordered in the vector $\hat{\mathbf{u}}(r,s)$ of $2n$ components

$$\hat{\mathbf{u}}(r,s) = \begin{bmatrix} \hat{u}_1^{(1)} & \hat{u}_2^{(1)} & .. & \hat{u}_1^{(n)} & \hat{u}_2^{(n)} \end{bmatrix}^T.$$

The second-order identitiy tensor, in array notation, has the form

$$\mathbf{I} = \begin{bmatrix} 1 & 1 & 1 & 0 & 0 \end{bmatrix}^T.$$

The $\mathcal{A}(\mathbf{H}_R)$ operator is a linear function that maps the components of $\mathbf{H}_R$ into the $5 \times 2n$ matrix and has the form

$$\mathcal{A}(\mathbf{H}_R) = \begin{bmatrix} (\mathbf{H}_R)_{11} & 0 & .. & (\mathbf{H}_R)_{1n} & 0 \\ 0 & (\mathbf{H}_R)_{21} & .. & 0 & (\mathbf{H}_R)_{2n} \\ 0 & 0 & .. & 0 & 0 \\ (\mathbf{H}_R)_{21} & 0 & .. & (\mathbf{H}_R)_{2n} & 0 \\ 0 & (\mathbf{H}_R)_{11} & .. & 0 & (\mathbf{H}_R)_{1n} \end{bmatrix}.$$

The operator $\mathcal{B}(\mathbf{H})$ is a linear function that maps the components of the matrix $\mathbf{H}$ into a $5 \times 2n$ matrix and has the form

$$\mathcal{B}(\mathbf{H}) = \begin{bmatrix} H_{11} & 0 & .. & H_{1n} & 0 \\ 0 & H_{21} & .. & 0 & H_{2n} \\ 0 & 0 & .. & 0 & 0 \\ \frac{1}{2}H_{21} & \frac{1}{2}H_{11} & .. & \frac{1}{2}H_{2n} & \frac{1}{2}H_{1n} \\ \frac{1}{2}H_{21} & \frac{1}{2}H_{11} & .. & \frac{1}{2}H_{2n} & \frac{1}{2}H_{1n} \end{bmatrix}.$$

E.2. 3D brick

The matrix $\mathbf{H}_p$ that contains the derivatives of the shape functions with respect to the intrinsic coordinate system $\mathbf{r}$, can be expressed as

$$\mathbf{H}_p = \begin{bmatrix} \frac{\mathrm{d}N^{(1)}}{\mathrm{d}r} & .. & \frac{\mathrm{d}N^{(n)}}{\mathrm{d}r} \\ \frac{\mathrm{d}N^{(1)}}{\mathrm{d}s} & .. & \frac{\mathrm{d}N^{(n)}}{\mathrm{d}s} \\ \frac{\mathrm{d}N^{(1)}}{\mathrm{d}t} & .. & \frac{\mathrm{d}N^{(n)}}{\mathrm{d}t} \end{bmatrix}.$$

The jacobian, in the reference coordinate system, can be computed as

$$\mathbf{J}_R = \mathbf{H}_p \hat{\mathbf{X}}_R,$$

where

$$\hat{\mathbf{X}}_R = \begin{bmatrix} \hat{x}_{R,1}^{(1)} & \hat{x}_{R,2}^{(1)} & \hat{x}_{R,3}^{(1)} \\ .. & .. & .. \\ \hat{x}_{R,1}^{(n)} & \hat{x}_{R,2}^{(n)} & \hat{x}_{R,3}^{(n)} \end{bmatrix}.$$

The nodal displacements are ordered in the vector $\hat{\mathbf{u}}(r,s,t)$ of $3n$ components

$$\hat{\mathbf{u}}(r,s,t) = \begin{bmatrix} \hat{u}_1^{(1)} & \hat{u}_2^{(1)} & \hat{u}_3^{(1)} & .. & \hat{u}_1^{(n)} & \hat{u}_2^{(n)} & \hat{u}_3^{(n)} \end{bmatrix}^T.$$

The second-order identity tensor, in array notation, has the form

$$\mathbf{I} = \begin{bmatrix} 1 & 1 & 1 & 0 & 0 & 0 & 0 & 0 & 0 \end{bmatrix}^T.$$

The $\mathcal{A}(\mathbf{H}_R)$ operator is a linear function that maps the components of $\mathbf{H}_R$ into the $9 \times 3n$ matrix and has the form

$$\mathcal{A}(\mathbf{H}_R) = \begin{bmatrix} (\mathbf{H}_R)_{11} & 0 & 0 & .. & (\mathbf{H}_R)_{1n} & 0 & 0 \\ 0 & (\mathbf{H}_R)_{21} & 0 & .. & 0 & (\mathbf{H}_R)_{2n} & 0 \\ 0 & 0 & (\mathbf{H}_R)_{31} & .. & 0 & 0 & (\mathbf{H}_R)_{3n} \\ (\mathbf{H}_R)_{21} & 0 & 0 & .. & (\mathbf{H}_R)_{2n} & 0 & 0 \\ (\mathbf{H}_R)_{31} & 0 & 0 & .. & (\mathbf{H}_R)_{3n} & 0 & 0 \\ 0 & (\mathbf{H}_R)_{31} & 0 & .. & 0 & (\mathbf{H}_R)_{3n} & 0 \\ 0 & (\mathbf{H}_R)_{11} & 0 & .. & 0 & (\mathbf{H}_R)_{1n} & 0 \\ 0 & 0 & (\mathbf{H}_R)_{11} & .. & 0 & 0 & (\mathbf{H}_R)_{1n} \\ 0 & 0 & (\mathbf{H}_R)_{21} & .. & 0 & 0 & (\mathbf{H}_R)_{2n} \end{bmatrix}.$$

The operator $\mathcal{B}(\mathbf{H})$ is a linear function that maps the components of the matrix $\mathbf{H}$ into a $9 \times 3n$ matrix and has the form

$$\mathcal{B}(\mathbf{H}_R) = \begin{bmatrix} (\mathbf{H}_R)_{11} & 0 & 0 & .. & (\mathbf{H}_R)_{1n} & 0 & 0 \\ 0 & (\mathbf{H}_R)_{21} & 0 & .. & 0 & (\mathbf{H}_R)_{2n} & 0 \\ 0 & 0 & (\mathbf{H}_R)_{31} & .. & 0 & 0 & (\mathbf{H}_R)_{3n} \\ \frac{1}{2}(\mathbf{H}_R)_{21} & \frac{1}{2}(\mathbf{H}_R)_{11} & 0 & .. & \frac{1}{2}(\mathbf{H}_R)_{2n} & \frac{1}{2}(\mathbf{H}_R)_{1n} & 0 \\ \frac{1}{2}(\mathbf{H}_R)_{31} & 0 & \frac{1}{2}(\mathbf{H}_R)_{11} & .. & \frac{1}{2}(\mathbf{H}_R)_{3n} & 0 & \frac{1}{2}(\mathbf{H}_R)_{1n} \\ 0 & \frac{1}{2}(\mathbf{H}_R)_{31} & \frac{1}{2}(\mathbf{H}_R)_{21} & .. & 0 & \frac{1}{2}(\mathbf{H}_R)_{3n} & \frac{1}{2}(\mathbf{H}_R)_{2n} \\ \frac{1}{2}(\mathbf{H}_R)_{21} & \frac{1}{2}(\mathbf{H}_R)_{11} & 0 & .. & \frac{1}{2}(\mathbf{H}_R)_{2n} & \frac{1}{2}(\mathbf{H}_R)_{1n} & 0 \\ \frac{1}{2}(\mathbf{H}_R)_{31} & 0 & \frac{1}{2}(\mathbf{H}_R)_{11} & .. & \frac{1}{2}(\mathbf{H}_R)_{3n} & 0 & \frac{1}{2}(\mathbf{H}_R)_{1n} \\ 0 & \frac{1}{2}(\mathbf{H}_R)_{31} & \frac{1}{2}(\mathbf{H}_R)_{21} & .. & 0 & \frac{1}{2}(\mathbf{H}_R)_{3n} & \frac{1}{2}(\mathbf{H}_R)_{2n} \end{bmatrix}.$$

Appendix F. Useful derivatives

$$\partial \bar{\mathbf{B}}_e^* / \partial \mathbf{F} = J_r^{-2/3} \left[\partial \mathbf{B}_e^* / \partial \mathbf{F} - \frac{2}{3} \left(\mathbf{F}_r \bar{\mathbf{B}}_e(t_n) \mathbf{F}_r{}^T \right) \otimes \mathbf{F}^{-T} \right], \tag{F.1}$$

where

$$\partial \left(\mathbf{B}_e^* \right)_{ij} / \partial (\mathbf{F})_{hk} = \delta_{ih} \left(\mathbf{F}(t_n)^{-1} \right)_{kq} \left(\tilde{\mathbf{B}}_e(t_n) \right)_{qs} \left(\mathbf{F}_r \right)_{js} + \delta_{jh} \left(\mathbf{F}_r \right)_{iq} \left(\tilde{\mathbf{B}}_e(t_n) \right)_{qs} \left(\mathbf{F}(t_n)^{-1} \right)_{ks}, \tag{F.2}$$

with $(\mathbf{A})_{ij} = \mathbf{A} \cdot \mathbf{e}_i \otimes \mathbf{e}_j$ being the components of the second-order tensor $\mathbf{A}$ relative to the orthonormal base vectors $\mathbf{e}_i$. Also, $\tilde{\mathbf{B}}_e(t_n)$ equals either $\bar{\mathbf{B}}_e(t_n)$ for the B_e model or $\mathbf{B}_e(t_n)$ for the LN and LN-MD models.

References

[1] J. Argyris, M. Kleiber, Incremental formulation in nonlinear mechanics and large strain elasto-plasticity – natural approach. part 1, Comput. Method. Appl. M. 11 (1977) 215–247. https://doi.org/10.1016/0045-7825(77)90060-3.

[2] Y. Bai, T. Wierzbicki, A new model of metal plasticity and fracture with pressure and lode dependence, Int. J. Plastic. 24 (2008) 1071–1096. https://doi.org/10.1016/j.ijplas.2007.09.004.

[3] J.P. Bardet, Lode dependences for isotropic pressure-sensitive elastoplastic materials, J. Appl. Mech.-T ASME 57 (1990) 498–506. https://doi.org/10.1115/1.2897051.

[4] I. Barsoum, J. Faleskog, Rupture mechanisms in combined tension and shear - experiments, Int. J. Solids Struct. 44 (2007) 1768–1786. https://doi.org/10.1016/j.ijsolstr.2006.09.031.

[5] I. Barsoum, J. Faleskog, Rupture mechanisms in combined tension and shear - micromechanics, Int. J. Solids Struct. 44 (2007) 5481–5498. https://doi.org/10.1016/j.ijsolstr.2007.01.010.

[6] B. Bernstein, Hypo-elasticity and elasticity, Arch. Ration. Mech. An. 6 (1960) 89–104. https://doi.org/10.1007/BF00276156.

[7] D. Bigoni, A. Piccolroaz, Yield criteria for quasibrittle and frictional materials, Int. J. Solids Struct. 41 (2004) 2855–2878. https://doi.org/10.1016/j.ijsolstr.2003.12.024.

[8] B.A. Bilby, L.R.T. Gardner, A.N. Stroh, Continuous distributions of dislocations and the theory of plasticity, In: Proceedings of the 9th International Congress of Applied Mechanics. University de Brussels 9 (1957) 35–44.

[9] C. Coulomb, Essai sur une application des règles de maximum et minimum, 1776.

[10] D. Systèmes, ABAQUS User's & Theory Manuals — Release 6.24, 2024. Providence, RI, USA.

[11] E.A. de Souza Neto, D. Perić, D.R.J. Owen, Computational Methods for Plasticity, John Wiley & Sons, Ltd, Chichester, UK, 2008.

[12] C. Eckart, The thermodynamics of irreversible processes. iv. the theory of elasticity and anelasticity, Phys. Rev. 73 (1948) 373–382. https://doi.org/10.1103/PhysRev.73.373.

[13] H.A.M. van Eekelen, Isotropic yield surface in three dimensions for use in soil mechanics, Int. J. Numer. Anal. Met. 4 (1980) 89–101. https://doi.org/10.1002/nag.1610040107.

[14] X. Gao, J. Kim, Modeling of ductile fracture: significance of void coalescence, Int. J. Solid. Struct. 43 (2006) 6277–6293. https://doi.org/10.1016/j.ijsolstr.2005.08.008.

[15] M. Geers, Finite strain logarithmic hyperelasto-plasticity with softening: a strongly non-local implicit gradient framework, Comput. Method. Appl. M. 193 (2004) 3377–3401. https://doi.org/10.1016/j.cma.2003.07.014.

[16] A.E. Green, P.M. Naghdi, A general theory of an elastic-plastic continuum, Arch. Ration. Mech. An. 18 (1965) 251–281. https://doi.org/10.1007/BF00251666.

[17] A.L. Gurson, Continuum theory of ductile rupture by void nucleation and growth: part I–Yield criteria and flow rules for porous ductile media, J. Eng. Mater.-T. ASME 99 (1977) 2–15. https://doi.org/10.1115/1.3443401.

[18] K. Heiduschke, Generalized strain space formulations and eigenprojection tensors, Acta Mech. 230 (2019) 3379–3422. https://doi.org/10.1007/s00707-019-02447-2.

[19] H. Hencky, The elastic behavior of vulcanized rubber, J. Appl. Mech.-T ASME 1 (1933) 45–48. https://doi.org/10.1115/1.4012174.

[20] H. Hibbitt, P. Marcal, J. Rice, A finite element formulation for problems of large strain and large displacement, Int. J. Solid. Struct. 6 (1970) 1069–1086. https://doi.org/10.1016/0020-7683(70)90048-X.

[21] R. Hill, A general theory of uniqueness and stability in elastic-plastic solids, J. Mech. Phys. Solid. 6 (1958) 236–249. https://doi.org/10.1016/0022-5096(58)90029-2.

[22] G. Houlsby, A general failure criterion for frictional and cohesive materials, Soil. Found. 26 (1986) 97–101. https://doi.org/10.3208/sandf1972.26.2_97.

[23] M. Jabareen, Strongly objective numerical implementation and generalization of a unified large inelastic deformation model with a smooth elastic–inelastic transition, Int. J. Eng. Sci. 96 (2015) 46–67. https://doi.org/10.1016/j.ijengsci.2015.07.001.

[24] J.C. Jaeger, N.G.W. Cook, Fundamentals of rock mechanics, Chapman and Hall, London, 1979.

[25] Y. Jiao, J. Fish, Is an additive decomposition of a rate of deformation and objective stress rates passé? Comput. Method. Appl. M. 327 (2017) 196–225. https://doi.org/10.1016/j.cma.2017.07.021.

[26] Y. Jiao, J. Fish, On the equivalence between the multiplicative hyper-elasto-plasticity and the additive hypo-elasto-plasticity based on the modified kinetic logarithmic stress rate, Comput. Method. Appl. M. 340 (2018) 824–863. https://doi.org/10.1016/j.cma.2018.06.017.

[27] C. Jog, The explicit determination of the logarithm of a tensor and its derivatives, J. Elast. 93 (2008) 141–148. https://doi.org/10.1007/s10659-008-9169-x.

[28] E. Kröner, General continuum theory of dislocations and intrinsic stresses, Arch. Ration. Mech. An. 4 (1959) 273–334. https://doi.org/10.1007/BF00281393.

[29] M. Kroon, J. Faleskog, Numerical implementation of a j_2- and j_3-dependent plasticity model based on a spectral decomposition of the stress deviator, Comput. Mech. 52 (2013) 1059–1070. https://doi.org/10.1007/s00466-013-0863-6.
[30] S. Kumar, B.P. Patel, Two novel alternative integration schemes for multi-invariants dependent isotropic finite deformation plasticity, Eur. J. Mech. A-Solid. 100 (2023) 105012. https://doi.org/10.1016/j.euromechsol.2023.105012.
[31] P.V. Lade, Elasto-plastic stress-strain theory for cohesionless soil with curved yield surfaces, Int. J. Solid. Struct. 13 (1977) 1019–1035. https://doi.org/10.1016/0020-7683(77)90073-7.
[32] P.V. Lade, Three-parameter failure criterion for concrete, J. Eng. Mech. Div.-ASCE 108 (1982) 850–863. https://doi.org/10.1061/JMCEA3.0002874.
[33] P.V. Lade, J.M. Duncan, Cubical triaxial tests on cohesionless soil, J. Soil Mech. Found. Div.-ASCE 99 (1973) 793–812. https://doi.org/10.1061/JSFEAQ.0001934.
[34] P.V. Lade, J.M. Duncan, Elasto plastic stress-strain theory for cohesionless soil, J. Geotech. Eng.-ASCE 101 (1975) 1037–1053. https://doi.org/10.1061/AJGEB6.0000204.
[35] R. Lagioia, A. Panteghini, The influence of the plastic potential on plane strain failure, Int. J. Num. Meth. Eng. 38 (2014) 844–862. https://doi.org/10.1002/nag.2236.
[36] R. Lagioia, A. Panteghini, On the existence of a unique class of yield and failure criteria comprising Tresca, von Mises, Drucker-Prager, Mohr-Coulomb, Galileo-Rankine, Matsuoka-Nakai and Lade-Duncan, Proc. R. Soc. A 472 (2016) 20150713. https://doi.org/10.1098/rspa.2015.0713.
[37] R. Lagioia, A. Panteghini, A.M. Puzrin, The I_3 generalization of the Galileo-Rankine tension criterion, Proc. R. Soc. A 470 (2014) 20140568. https://doi.org/10.1098/rspa.2014.0568.
[38] E.H. Lee, Elastic-plastic deformation at finite strains, J. Appl. Mech.-T ASME 36 (1969) 1–6. https://doi.org/10.1115/1.3564580.
[39] A.I. Leonov, Nonequilibrium thermodynamics and rheology of viscoelastic polymer media, Rheol. Acta 15 (1976) 85–98. https://doi.org/10.1007/BF01517499.
[40] W. Lode, Versuche über den Einfluss der mittleren Hauptspannung auf das Fliessen der Metalle Eisen, Kupfer, und Nickle, Z. Physik 36 (1926) 913–939. https://doi.org/10.1007/BF01400222.
[41] C.P. Luehr, M.B. Rubin, The significance of projection operators in the spectral representation of symmetric second order tensors, Comput. Method. Appl. M. 84 (1990) 243–246. https://doi.org/10.1016/0045-7825(90)90078-Z.
[42] H. Matsuoka, T. Nakai, Stress-deformation and strength characteristics of soil under three different principal stresses, Proc. JSCE 232 (1974) 59–70. https://doi.org/10.2208/jscej1969.1974.232_59.
[43] R. McMeeking, J. Rice, Finite-element formulations for problems of large elastic-plastic deformation, Int. J. Solid. Struct. 11 (1975) 601–616. https://doi.org/10.1016/0020-7683(75)90033-5.
[44] O. Mohr, Welche Umstände bedingen die Elastizitätsgrenze und den Bruch eines Materials? Zeit des Ver Deut Ing 44 (1900) 1524–1530.
[45] J.C. Nagtegaal, J.E. De Jong, Some computational aspects of elastic-plastic large strain analysis, Int. J. Num. Meth. Eng. 17 (1981) 15–41. https://doi.org/10.1002/nme.1620170103.
[46] K. Nahshon, J. Hutchinson, Modification of the Gurson model for shear failure, Eur. J. Mech. A-Solid. 27 (2008) 1–17. https://doi.org/10.1016/j.euromechsol.2007.08.002.
[47] E.T. Onat, The notion of state and its implications in thermodynamics of inelastic solids, in: Irreversible Aspects of Continuum Mechanics and Transfer of Physical Characteristics in Moving Fluids: Symposia Vienna, June 22–28, 1966, Springer, 1968. 292–314.
[48] N.S. Ottosen, A failure criterion for concrete, J. Eng. Mech. 103 (1977) 527–535. https://doi.org/10.1061/JMCEA3.0002248.
[49] A. Panteghini, An analytical solution for the estimation of the drawing force in three dimensional plate drawing processes, Int. J. Mech. Sci. 84 (2014) 147–157. https://doi.org/10.1016/j.ijmecsci.2014.04.012.
[50] A. Panteghini, A simple spectral representation of a second-order symmetric tensor and its variation, Eur. J. Mech. A-Solid. 104 (2024) 105208. https://doi.org/10.1016/j.euromechsol.2023.105208.
[51] A. Panteghini, R. Lagioia, A fully convex reformulation of the original Matsuoka-Nakai failure criterion and its implicit numerically efficient integration algorithm, Int. J. Numer. Anal. Met. 38 (2014) 593–614. https://doi.org/10.1002/nag.2228.
[52] A. Panteghini, R. Lagioia, An approach for providing quasi-convexity to yield functions and a generalized implicit integration scheme for isotropic constitutive models based on 2 unknowns, Int. J. Numer. Anal. Met. 42 (2018) 829–855. https://doi.org/10.1002/nag.2767.
[53] A. Panteghini, R. Lagioia, An implicit integration algorithm based on invariants for isotropic elasto-plastic models of the cosserat continuum, Int. J. Numer. Anal. Met. 46 (2022) 2233–2267. https://doi.org/10.1002/nag.3386.
[54] D. Perić, On consistent stress rates in solid mechanics: Computational implications, Int. J. Num. Meth. Eng. 33 (1992) 799–817. https://doi.org/10.1002/nme.1620330409.
[55] A. Piccolroaz, D. Bigoni, Yield criteria for quasibrittle and frictional materials: a generalization to surfaces with corners, Int. J. Solids Struct. 46 (2009) 3587–3596. https://doi.org/10.1016/j.ijsolstr.2009.06.006.
[56] J. Podgórski, General failure criterion for isotropic media, J. Eng. Mech. 111 (1985) 188–201. https://doi.org/10.1061/(ASCE)0733-9399(1985)111:2(188).
[57] R.S. Rivlin, G.I. Barenblatt, Collected papers of RS Rivlin, Springer Science & Business Media, 1, 1997.
[58] M.B. Rubin, Simple, convenient isotropic failure surface, J. Eng. Mech. 117 (1991) 348–369. https://doi.org/10.1061/(ASCE)0733-9399(1991)117:2(348).
[59] M.B. Rubin, Plasticity theory formulated in terms of physically based microstructural variables – part I. Theory, Int. J. Solid. Struct. 31 (1994) 2615–2634. https://doi.org/10.1016/0020-7683(94)90222-4.
[60] M.B. Rubin, Removal of unphysical arbitrariness in constitutive equations for elastically anisotropic nonlinear elastic–viscoplastic solids, Int. J. Eng. Sci. 53 (2012) 38–45. https://doi.org/10.1016/j.ijengsci.2011.12.008.
[61] M.B. Rubin, Continuum Mechanics with Eulerian Formulations of Constitutive Equations, Springer Nature, 2021.
[62] M.B. Rubin, Erratum for “Simple, convenient isotropic failure surface” by M.B. Rubin, J. Eng. Mech. 147 (2021) 08220002. https://doi.org/10.1061/(ASCE)EM.1943-7889.0001874.
[63] M.B. Rubin, A.V. Attia, Calculation of hyperelastic response of finitely deformed elastic-viscoplastic materials, Int. J. Num. Meth. Eng. 39 (1996) 309–320. https://doi.org/10.1002/(SICI)1097-0207(19960130)39:2<309::AID-NME858>3.0.CO;2-B.
[64] M.B. Rubin, L. Bardella, Eulerian rates of elastic incompatibilities applied to size-dependent hardening in finite torsion, J. Mech. Phys. Solid. 193 (2024) 105905. https://doi.org/10.1016/j.jmps.2024.105905.
[65] M.B. Rubin, P. Cardiff, Advantages of formulating an evolution equation directly for elastic distortional deformation in finite deformation plasticity, Comput. Mech. 60 (2017) 703–707. https://doi.org/10.1007/s00466-017-1434-z.
[66] M.B. Rubin, O. Papes, Advantages of formulating evolution equations for elastic-viscoplastic materials in terms of the velocity gradient instead of the spin tensor, J. Mech. Mater. Struct. 6 (2011) 529–543. https://doi.org/10.2140/jomms.2011.6.529.
[67] R. Salgado, V. Bisht, Advances in the solution of geotechnical boundary-value problems, Comput. Geotech. 138 (2021) 104183. https://doi.org/10.1016/j.compgeo.2021.104183.
[68] J.C. Simo, A framework for finite strain elastoplasticity based on maximum plastic dissipation and the multiplicative decomposition. part I: continuum formulation, Comput. Method. Appl. M. 66 (1988) 199–219. https://doi.org/10.1016/0045-7825(88)90076-X.
[69] J.C. Simo, A framework for finite strain elastoplasticity based on maximum plastic dissipation and the multiplicative decomposition. part II: computational aspects, Comput. Method. Appl. M. 68 (1988) 1–31. https://doi.org/10.1016/0045-7825(88)90104-1.
[70] J.C. Simo, Algorithms for static and dynamic multiplicative plasticity that preserve the classical return mapping schemes of the infinitesimal theory, Comput. Method. Appl. M. 99 (1992) 61–112. https://doi.org/10.1016/0045-7825(92)90123-2.
[71] J.C. Simo, Numerical analysis and simulation of plasticity, in: Numerical Methods for Solids (Part 3) Numerical Methods for Fluids (Part 1), 6 of Handbook of Numerical Analysis, Elsevier, 6, 1998, pp. 183–499. https://doi.org/10.1016/S1570-8659(98)80009-4.
[72] J.C. Simo, F. Armero, Geometrically non-linear enhanced strain mixed methods and the method of incompatible modes, Int. J. Num. Meth. Eng. 33 (1992) 1413–1449. https://doi.org/10.1002/nme.1620330705.

[73] J.C. Simo, C. Miehe, Associative coupled thermoplasticity at finite strains: formulation, numerical analysis and implementation, Comput. Method. Appl. M. 98 (1992) 41–104. https://doi.org/10.1016/0045-7825(92)90170-O.
[74] J.C. Simo, M. Ortiz, A unified approach to finite deformation elastoplastic analysis based on the use of hyperelastic constitutive equations, Comput. Method. Appl. M. 49 (1985) 221–245. https://doi.org/10.1016/0045-7825(85)90061-1.
[75] J.C. Simo, K.S. Pister, Remarks on rate constitutive equations for finite deformation problems: computational implications, Comput. Method. Appl. M. 46 (1984) 201–215. https://doi.org/10.1016/0045-7825(84)90062-8.
[76] J.J. Sylvester, Sur l'équations en matrices px = xq, Comptes Rendus Acad. Sci. 99 (1884) 67–71, 115,116.
[77] H. Tresca, Mémoire sur l'écoulement des corps solides, 1868.
[78] V.V. Vershinin, A correct form of Bai-Wierzbicki plasticity model and its extension for strain rate and temperature dependence, Int. J. Solid. Struct. 126–127 (2017) 150–162. https://doi.org/10.1016/j.ijsolstr.2017.08.001.
[79] K.J. William, E.P. Warnke, Constitutive model for the triaxial behavior of concrete, In: Proceedings of IABSE, Structural Engineering Report 19, Section III (1975) 1–30.
[80] M. Zecevic, M. Cawkwell, D. Luscher, Eulerian finite element implementations of a dislocation density-based continuum model, Int. J. Solid. Struct. 288 (2024) 112590. https://doi.org/10.1016/j.ijsolstr.2023.112590.
[81] L. Zhan, S.Y. Wang, O.T. Bruhns, H. Xiao, High-efficiency algorithms for simulating metal failure effects under multiaxial repeated loadings, Int. J. Num. Meth. Eng. 123 (2022) 1277–1293. https://doi.org/10.1002/nme.6895.